Final Report

Project Title:	How grain boundaries affect the efficiency of poly-CdTe solar-cells: A fundamental atomic-scale study of grain boundary dislocation cores using CdTe bi-crystal thin films.
Project Period:	01/01/13– 08/16/16
Project Budget:	$903,044
Submission Date:	09/13/16
Recipient:	University of Illinois at Chicago
Recipient DUNS #:	098987217
Address:	809 S. Marshfield Ave Chicago, IL 60612
Website (if available)	www.uic.edu
Award Number:	DE-EE0005956
Awarding Agency:	DOE EERE Sunshot
Working Partners:	University of Texas at Dallas, Argonne National Laboratory

Principal Investigator: Robert F Klie
Professor of Physics
Phone: 312-996-6064
Fax: 312-996-9016
Email: rfklie@uic.edu

A. EXECUTIVE SUMMARY

It is now widely accepted that grain boundaries in poly-crystalline CdTe thin film devices have a detrimental effect on the minority carrier lifetimes, the open circuit voltage and therefore the overall solar-cell performance. The goal of this project was to develop a fundamental understanding of the role of grain boundaries in CdTe on the carrier life-time, open-circuit voltage, V_{oc}, and the diffusion of impurities. To achieve this goal, i) CdTe bi-crystals were fabricated with various misorientation angels, ii) the atomic- and electronic structures of the grain boundaries were characterized using scanning transmission electron microscopy (STEM), and iii) first-principles density functional theory modeling was performed on the structures determined by STEM to predict the grain boundary potential. The transport properties and minority carrier lifetimes of the bi-crystal grain boundaries were measured using a variety of approaches, including TRPL, and provided feedback to the characterization and modeling effort about the effectiveness of the proposed models.

Over the last 42 months, this project has established that CdTe bi-crystals can be fabricated and characterized using a variety of methods. Moreover, it was demonstrated that bi-crystals offer a model system to analyze the effects of dislocation cores on the minority carrier lifetimes and grain boundary potentials. The role of $CdCl_2$ passivation, as well as several other post deposition treatment in poly-crystalline CdTe were tested on the bi-crystal systems and their effect on the local atomic and electronic structures was determined.

The major knowledge obtained about CdTe in this project:

1. The process of fabricating CdTe bi-crystals as model systems for grain boundaries in poly-crystalline CdTe solar cells.
2. The atomic-structure of structural units in CdTe grain boundaries and their influence on the local density of states.
3. The suppression of carrier lifetimes at the grain boundary and the extend of this suppression into the CdTe bulk.
4. The location and influence of Cl at the CdTe grain boundary.

As part of this project, the PIs developed a grain boundary software tool, that will allow the user to construct a random-angle grain boundary in CdTe and determine the atomic-structure using empirical parameter, such ion-radius and minimum bond-length. This program is now available at the Argonne National Laboratory User Center.

This work sets the stage for developing a more general grain boundary model that can lead to the ability to determine the effects of the grain boundary network on the transport and energy conversion efficiency of poly-crystalline CdTe devices. Moreover, once the precise role of grain boundaries in limiting the carrier lifetimes and open circuit voltage is known, more effective passivation approaches can be developed to eliminate their detrimental effects. Such an effort will ultimately lead to the optimization of poly-crystalline CdTe devices approaching the theoretical limit of 30%.

Table of Contents

B. BACKGROUND

Poly-CdTe PV modules have the lowest commercial manufacturing costs ($/W) in today's solar industry. However, in order to further reduce these costs, the module efficiency will need to be brought well above 22%, with system lifetimes in excess of 30 years. Higher efficiency modules are also important for lowering balance of system costs, which is essential to bring the levelized cost of electricity (LCOE) below the target of $0.03/kWh by the year 2030. A poly-CdTe PV record efficiency of 22.1% was recently demonstrated by First Solar, Inc.[1] However, such cell performances are still far from the theoretical limits (~30% for CdTe), and improvements have mostly been due to better light collection, rather than improvements in absorber conversion efficiency. Improvements in absorber conversion efficiency are often achieved by increasing the Cu concentration at the back contact to minimize the contact barrier. High Cu-concentrations will, however, lead to an increased rate of cell degradation over time, driven mostly by V_{oc} and fill-factor losses.[2, 3] On the other hand, too little Cu will result in low cell efficiency due to a back contact barrier, but more long-term device stability. The highest open-circuit voltage (V_{oc}) of 850 mV was demonstrated in 1994 [4] and largely remains unchanged to date. Recent short circuit current density (J_{sc}) improvements have primarily been obtained through improvements in the transparent conductive oxide (TCO) layer. However, the majority of the J_{sc} loss remaining is due to the CdS layer. In order to significantly improve thin film CdTe efficiency to meet grid parity levelized cost of electricity (LCOE), significant breakthrough advances need to be made to increase the minority carrier lifetime, and V_{oc} .[5]

In recent years, it has become increasingly clear that minority carrier life-time and doping activation impose a fundamental limit to improving the efficiency of poly-CdTe solar-cell devices beyond the current state-of-the-art of 22.1%. However, such a breakthrough can no longer be achieved by incremental engineering improvement to the cell design. On the contrary, a fundamental understanding of the defect and grain boundary structures in the poly-crystalline CdTe absorber layer is necessary to significantly increase the minority carrier lifetime, V_{oc} and J_{sc}, and thereby increase the entire module efficiency beyond 20%, as required by the SunShot Initiative.

The novel idea of this project was to fabricate grain boundaries in CdTe thin films with well-defined misorientation angles and examine their role on the transport properties CdTe. While there are plenty of grain boundaries in a single poly-crystalline CdTe thin-film device, it is impossible to measure the effects of grain boundaries separate from that of the bulk, the contacts or the superstrate. The grain boundaries for this project were instead fabricated using the bi-crystal method, where two single-crystal CdTe wafers are bonding at specific misorientation angles using high-temperature and high-pressure. While this method has been used for oxide thin films over the last few decades, no such bi-crystals have ever been made using II-VI semi-conductors.

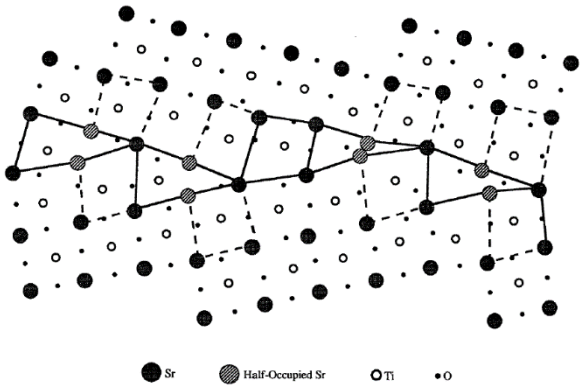

Figure 1: Structural model of a 25° (920) grain boundary in $SrTiO_3$. Structural units are indicated by the black lines. (Browning and Pennycook [7])

Since 1950, when Read and Shockley published their paper on dislocation models in

crystal grain boundaries,[6] the notion of structural units has been used to describe dislocation cores in crystalline grain boundaries. In 1996, Browning and Pennycook used a combination of high-resolution HAADF imaging and bond-valence analysis to identify a series of structural units in tilt grain boundaries of $SrTiO_3$, which contain partially occupied columns of Sr or Ti-O to accommodate the ionic repulsion (see Figure 1), thereby introducing the idea of non-stoichiometric structural units.[7] Using a series of symmetric and asymmetric [001] tilt grain boundaries with various misorientation angles, the authors identified six distinct structural units that can be arranged in different order to compose every tilt grain boundary in the range 0 – 90° with $\Sigma<41$.

Since then, the model of structural grain boundary units has been used to characterize tilt and twist grain boundaries, not just in $SrTiO_3$,[8] but also in other perovskite-like oxides, such as the high-temperature superconductor $YBa_2Cu_3O_7$,[9] or other oxides, such as α-Al_2O_3,[10] CeO_2, [11] or rutile TiO_2.[12] Moreover, first-principles calculations have been possible using such relatively simple structural units compared to the size of a supercell that would be necessary to model the entire grain boundary structure. Such calculations have demonstrated that grain boundaries in $SrTiO_3$ are intrinsically non-stoichiometric, with an excess of Ti and O vacancies present in the dislocation cores, which results in the formation of a grain boundary potential.[13]

The objective of this project was to demonstrate that well-controlled CdTe grain boundaries can be fabricated using the bi-crystal approach and that these grain boundaries have structures and properties similar to grain boundaries found in poly-crystalline devices. The presence of structural units, similar to those discovered in perovskite oxides, was confirmed next, and the density of states of the different structures was determined using a combination of atomic-resolution scanning transmission electron microscopy and first-principles modeling. Electronic transport and minority carrier lifetime measurements were conducted to provide feedback to the modeling effort and to compare the bi-crystal properties to those of poly-crystalline CdTe.

Prior to a detailed discussion of the outcomes of this project, we will briefly review the methods and approaches that were employed.

a) Ultra-high vacuum wafer bonding

An UHV wafer bonding unit, especially designed to use surface characterization and thin-film deposition techniques to measure and control substrate and interface chemistry within limits necessary to make heterojunction devices, is available to produce integrated heterostructures with well controlled chemistry that are tractable for quantitative nanostructural and properties measurements. This unit is capable of synthesizing interfaces by direct wafer bonding and/or in-situ thin film deposition methods, and offers greater flexibility for producing advanced integrated artificial structures. It consists of five interconnected ultra high vacuum (UHV) chambers for in-situ surface preparation and analysis, addition of interlayers by e-beam or UHV sputter deposition, a bonding chamber, and a sample entry and preparation chamber. The base pressure is $2x10^{-10}$ Torr. Orientation of the bonded pairs can be controlled to ~0.1 degree prior to bonding. It is straightforward to investigate relative orientation effects across interfaces. The maximum bonding temperature is ~1200˚C. Specimens are transferred between chambers for Auger electron spectroscopy (AES) and reflection high energy electron diffraction (RHEED) surface analysis and in-situ specimen surface preparation by ion bean cleaning and/or thermal desorption before bonding. Ex-situ surface preparations using etching and low energy reactive plasma cleaning is done in a clean room to protect substrates prior to insertion in the bonding instrument. Since both nanoscale and long range substrates flatness affect bonding, special surface preparation methods

were developed. An atomic force microscopy (AFM) was used to provide direct measurements of surface roughness.

The bi-crystal fabrication is done in a UHV or ultra-clean environment, which includes the cutting, polishing and bonding of the CdZnTe wafer substrates. The commercially available wafer of Cd1-xZnxTe (x=0, 0.05) in the [001] or [211] orientation is cut into two pieces, followed by polishing of one side to a specific misorientation angle. Subsequently, both faces of the cut are cleaned and bonded at high-temperature in UHV to form the new bi-crystal substrate.

b) Aberration-corrected scanning transmission electron microscopy (AC-STEM)

The atomic and electronic structures of the fabricated grain boundaries are characterized using the aberration-corrected scanning transmission electron microscope (AC-STEM) at the University of Illinois – Chicago (UIC). The JEOL ARM-200CF is a cold-field emission, electron probe aberration corrected STEM, equipped with a post-column electron energy-loss spectrometer (EELS), as well as several cameras. This setup will allow for atomic-resolution imaging with a probe-size of 68 pm and an energy-resolution of 350 meV at a primary electron energy of 200 kV. The ARM-200CF can also be operated at a primary electron energy of 80 kV without any substantial loss in resolution (78 pm and 350 meV). This setup is particularly helpful for energy-dispersive X-ray spectroscopy (XEDS), sine the scattering cross-section of atomic-columns is significantly increased at lower primary energy. In early 2013, the detector for back-scattered X-rays was replaced with a large area system. This upgrade provided a 10 fold increase in detected X-ray signal, and a 4 times large collection solid angle, allowing for atomic-resolution XEDS maps to be acquired in as little as 60 s.

The CdTe bi-crystal samples are prepared from the wafer-bonded materials using the focused ion-beam approach. More specifically, the FEI Nova 200 NanoLab focused ion beam system was used, which also serves as a dual column SEM. It combines ultra-high resolution field emission scanning electron microscopy (SEM) and focused ion beam (FIB) etch and deposition for nanoscale prototyping, machining, 2-D and 3-D characterization, and analysis. Five gas injection systems are available for deposition and etching. Nanoscale chemical analysis will be done with energy dispersive X-ray spectroscopy (EDS). The secondary electron image resolution at the dual beam coincidence point is 1.5 nm at 15 kV. The FIB optics has better than 7 nm resolution at 30 kV. A high-resolution digital patterning system controlled from the user interface is also available. Predefined device structures in bitmap format can be directly imported to the patterning system for nanoscale fabrication. The FEI Nova 200 is also equipped with a Zyvex F100 nano-manipulation stage, which includes four manipulators with 10 nm positioning resolution. The four manipulators can be fitted with either sharp whisker probes for electrically probing samples or micro-grippers for manipulating nanostructures as small as 10 nanometers. This is the first instrument of its kind in the world that combines a dual beam FIB with the F100 nano-manipulator, providing unparalleled nanofabrication and nano-manipulation.

c) CdTe thin film deposition using molecular beam epitaxy (MBE)

Pristine and *p*-type doped CdTe thin films were deposited using MBE. Four RIBER MBE growth systems were available for the thin film synthesis: a 3-inch Riber 32P MBE system, two Riber 2300 system, and a 5-inch Riber Opus system. These four machines offer great flexibility in the range of materials grown and in the *in situ* characterization techniques available to the grower. The Riber 32P MBE system is configured for the growth of HgCdTe layers and superlattices. This

chamber is equipped with a valved Hg cell and an As cracker cell for p-type doping. It is also equipped with a state-of-the-art Woollam M2000 Spectroscopic Ellipsometer capable of *in situ* measurement of the dielectric function of the growing surface in the spectral range of 0.7 to 5.0 eV. Two Riber 2300 systems are configurable for the growth of various materials including wide band II-VI and thin magnetic layers. Finally, the Riber Opus system is primarily configured for the growth of CdTe on large (up to 5 inch) Si substrates. The *in situ* characterization techniques attached to the four growth chambers include RHEED, spectroscopic ellipsometry, XPS, UPS, ELS, SIMS, and AES. A clean room which is constructed following the Federal Standard 209e Class 10K, contains all MBE chambers as well as three complete chemical hoods for sample preparation. In addition, MPL also has a radio frequency magnetron sputtering system, several thermal evaporation systems, as well as sol-gel and chemical deposition facilities for poly-crystalline or nano-scale crystalline film deposition or growth.

d) First-principles modeling using density functional theory

Atomistic models of dislocation cores were constructed using HAADF-STEM images. First, a black and white filter was applied on the raw HAADF-STEM image to remove the noise and enhance the bright spots located at atomic columns. The positions of bright spots that correspond to atomic columns were identified using image analysis techniques with the Scikit-Image package. To extract the coordinates of atomic columns corresponding to bright spots, we located the maximum peak intensities using a maximum filter with a determined threshold on the image. To remove multiple maximum peaks appearing between atomic columns, the nearest neighbors of each peak were calculated using a radius of 0.9 Å, and combined the peak locations that are closer than this value by taking the center of mass of the nearest neighbors of each peak. After locating the positions of atomic columns, the crystallographic information in the CdTe crystal was used to identify the separate Cd and Te columns and obtained the atomic structure. To build a periodic supercell, the structure was juxtaposed with its mirror image and created a dislocation dipole where necessary. Before first principles calculations, we relaxed the dislocation dipole structure using available Stillinger-Weber and bond order empirical potentials for CdTe. These calculations have lower computational costs compared to DFT calculations and enabled us to determine near-minimum-energy dislocation core structures which match well with the HAADF-STEM images. Many variations of atomic configuration at the dislocation cores were considered by adding/subtracting atoms and changing the dimensions of the supercell so that the dislocation cores are not strongly affected by the periodic boundary conditions imposed on the system. In all cases, both interatomic potentials relaxed the atoms to similar positions. The atomic coordinates in the dislocation models are further relaxed using DFT.

The electronic structure of dislocation cores was analyzed in terms of electronic density of states, charge transfer, and electrostatic potential change at and near the dislocation core using plane-wave-based density functional theory (DFT) method. All DFT calculations were carried out using Vienna Ab initio Simulation Package (VASP). Projector augmented wave (PAW) potentials were used, and the exchange-correlation was treated with the generalized gradient approximation (GGA) parameterized by Perdew, Burke, and Ernzerhof (PBE). Calculations were carried out at the Γ-point in the Brilluoin zone using plane-wave kinetic energy cutoff of 343 eV. Atomic positions were relaxed until forces are below 0.05 eV/Å and electronic relaxation was converged to 10^{-5} eV to ensure convergence to 1–2 meV/atom in total energy. The electronic charges on atoms in DFT calculations are obtained by partitioning the charge density according to atomic positions in the crystal based on the Bader charge analysis, as implemented in VTST-scripts. Some

DFT calculations are performed on Extreme Science and Engineering Discovery Environment (XSEDE) resources.

e) Other characterization measurements

Hall effect and other current-voltage measurement equipment (fully automated from 300 K down to 8 K) were conducted on the CdTe bi-crystals. I-V device characterization measurements were conducted at room temperature using a Keithley 4200 Cascade probe station. After wafer bonding, Pt contact pads with size of 50 x 50 μm^2 were deposited on the bi-crystal surface using FIB. The configuration of the Pt electrode were chosen to optimize the intra and inter-grain I-V characteristics. The I-V measurements were carried out on a Cascade probe station with a semiconductor characterization

Time-resolved photoluminescence (TRPL) measurements were conducted on several CdTe bi-crystals as well as bulk CdTe wafers. Such measurements can determine the local minority carrier lifetimes and detect spatial variations in the lifetimes. The TRPL measurements using a confocal imaging approach were conducted through a user-proposal at Lawrence-Berkeley National Laboratory (LBNL) under the supervision of E. Barnard and J. Schuck.

C. SUMMARY OF STATEMENT OF PROJECT OBJECTIVES, MILESTONES, AND GO/NO-GO POINTS

Budget Period 1:

Task 1: Fabrication of CdTe Bi-crystals

We have successfully fabricated various low and high-angle CdTe grain boundaries, including both twist and tilt misorientation angle interfaces using the wafer bonding technique. Upon evaluating different bonding conditions for successful integration with minimal or no interfacial layers, the optimized bonding conditions resulted in well-bonded interfaces despite the large surface roughness of as-received CdTe single crystals. The electrical properties across the bonded interfaces were successfully measured and compared with that of the CdTe single crystal.

Subtask 1.1: Fabrication of small angle tilt grain boundaries

We initially evaluated several commercial CdTe single crystal wafers for our proposed bi-crystal fabrications and found that the surface roughness of the as-received CdTe (111) wafers was too severe to be used for successful bi-crystal bonding. We have developed an optimized chemical cleaning recipe consisting of a DI water rinse, 15% HCl, DI water rinse followed by drying at 110°C to achieve a smoother and cleaner surface. Using these CdTe wafers, we tested several bonding conditions, and found that thermal compression bonding at 400°C with 1 MPa pressure resulted in sharp and straight bonded CdTe interfaces.

Using these conditions, we have since successfully fabricated low-angle tilt and twist grain boundaries, including a 4° (110) tilt grain boundary, where the individual dislocation core at the interface are separated by several nanometers of bulk CdTe. These bi-crystal samples were then

cut for STEM analysis (see **Task 3**), MBE synthesis (see **Task 2**) and for I-V measurements. For a complete set of fabricated grain boundaries, see Table 1.

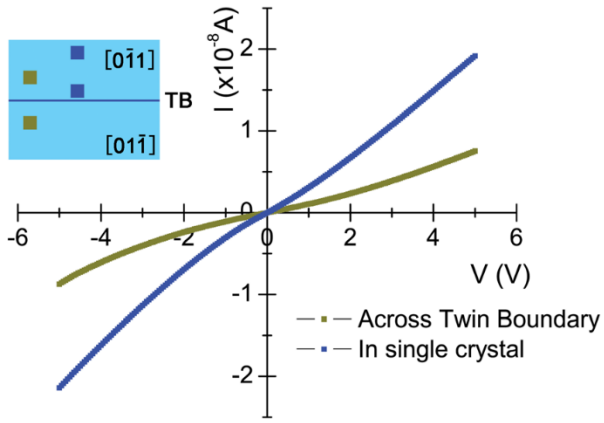

Figure 2: I-V characteristics from CdTe single crystal and across bonded twin boundary. The inset shows the electrical connection configurations. The Pt electrodes, shown as dark yellow and blue, were used for the I-V measurement of the twin boundary and single crystal, respectively.

Table 1: Summary of bonded interfaces.

Wafer Plane	**Bonded Orientation**	**Remarks**
CdTe (100)	$[011]_1//[011]_2$	Well bonded
CdTe (111)	$[112]_1//[011]_2$	Well bonded
	$[0\text{-}11]_1//[01\text{-}1]_2$	Well bonded
	2° tilt	Well bonded
	5° tilt	Well bonded
CdTe (110)	$[101]_1//[101]_2$	Well bonded
	4° tilt	Well bonded
CdTe (211)	$[0\text{-}11]_1//[01\text{-}1]_2$	Well bonded, with an interfacial layer
CdZnTe (111)	$[0\text{-}11]_1//[011]_2$	Well bonded, with an interfacial layer

Subtask 1.2: Fabricate high angle tilt grain boundaries

As part of this subtask, we have fabricated several large angle twist grain boundaries. High-angle tilt grain boundaries were fabricated during the Budget Period 2. However, I-V measurement have been conducted on the high-angle twist boundaries. Generally, it is difficult to obtain the electronic transport properties across the single twin boundary in poly-crystalline materials, such

as CdTe solar-cell devices, due to the limited size of the grains. In contrast, the CdTe bi-crystals fabricated by wafer bonding offer several millimeters of single crystal wafers to deposit ohmic contacts. The electrical properties across a twin boundary and of the single crystal are shown in the *I-V* charateristics of Figure 2. Pt electrodes, shown in dark yellow and bule, were used for the *I-V* measurement for twin boundary and single crystal, respectively. The slight nonlinear curve of single crystal (blue) curve as shown in Figure 2, indicated the non-ohimc contact of the Pt/CdTe interface. The *I-V* curve across the twin boundary becomes increasingly nonlinear with increasing voltage, which indicates the presence of a potential barrier at the bonded twin boundary. This measurement is in agreement with experimental and theoretical resutls from other III-V and II-VI semiconductor devices.

Task 2: Synthesis of *p*-type doped CdTe thin films

Doped CdTe films were successfully grown during Budget Period 1. Single-crystal CdTe layers doped with As were grown with a carrier concentration in excess of 10^{15} cm^{-3} using molecular beam epitaxy. Doped CdTe layers containing large angle twist grain boundaries (i.e. twin boundaries) were synthesized and characterized.

Subtask 2.1: Synthesize doped CdTe on small angle grain boundary substrates

The growth of high-quality CdTe films on CdTe substrates is significantly more challenging than the more common growth on Si substrates. In particular, the sample mounting and oxide desorb steps need adjustment from the standard growth recipe. To this end, the process outlined in Figure 3 has been developed for bulk CdTe epitaxial regrowth.

A quick bromine/methanol etch leaves a clean, Te rich surface. The sample is then mounted to a molybdenum holder and inserted in to the chamber. Once in the growth chamber, an initial desorb step at > 350° C removes the Te and any oxide that has formed. The removal of these surface layers can be monitored in-situ via RHEED. The substrate is then returned to the growth temperature and growth is commenced.

High doping is required both for increasing the V_{oc} of photovoltaic devices, and for facilitating electrical characterization techniques. In order to demonstrate p-type extrinsic doping, MPL has undertaken a study of As doping of MBE CdTe. We have successfully demonstrated doping up to 10^{16} cm^{-3} using an arsenic cracker source, and greater the 5 x 10^{15} cm^{-3} using a Cd_3As_2 source (see Figure 4). Comparison of SIMS and Hall data show increased activation efficiencies associated with the Cd_3As_2 source, most likely due to the increased cation overpressure facilitating

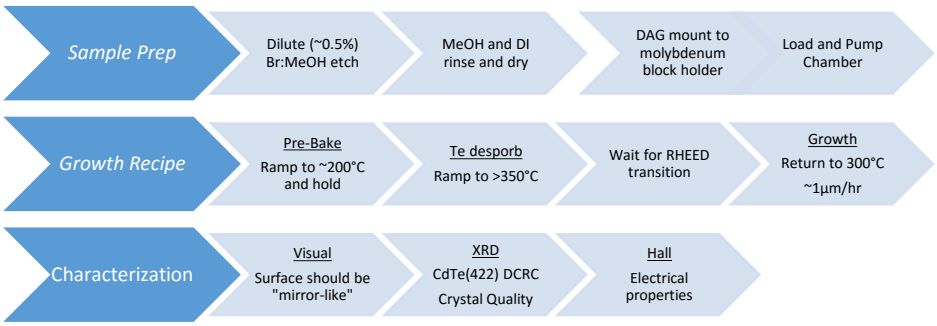

Figure 3: Standard MBE CdTe regrowth process.

Te-site incorporation of As. Samples grown with either source required a post-growth annealing > 480° C for activation.

We are confident in our abilities to dope to ~ 10^{16} cm^{-3} in epitaxial CdTe films, and identification of limiting factors in our epitaxial regrowth on bulk substrates clears the way to successfully overcoming the obstacles encountered thus far. We have modified our sample preparation procedure by adding an additional mechanical polishing step for as-received substrates, and are recommending (211) orientation for future substrates.

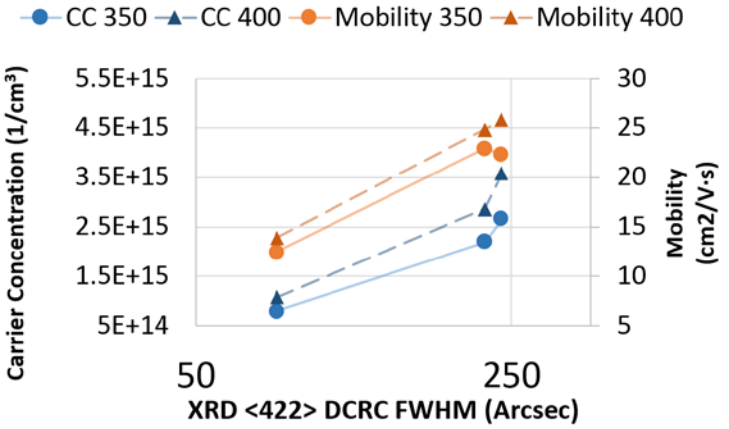

Figure 4: Carrier concentration and Hall mobility of p-type doped CdTe single-crystal layers grown by MBE.

Task 3: Atomic-scale characterization of CdTe grain boundaries

Atomic-scale characterization of CdTe bi-crystal interfaces with both twist and tilt misorientation angles was performed. Atomic-resolution Z-contrast imaging coupled with atomically-resolved X-ray spectrum imaging revealed structures of dislocation cores at these interfaces. Associated strain-fields were investigated via geometrical phase analysis. In addition, stoichiometry of twins within poly-crystalline CdTe thin films were analyzed using atomic-resolution Z-contrast imaging and electron energy-loss spectroscopy, and was correlated to the post-growth $CdCl_2$ treatment. The lowest elastic-energy edge dislocation junctions and their formation mechanisms were also investigated. The analysis has turned out helpful in interpretation of the discrete arrays of dislocations composing the low-angle tilt grain boundary.

Subtask 3.1: Atomic-resolution characterization of low angle grain boundaries

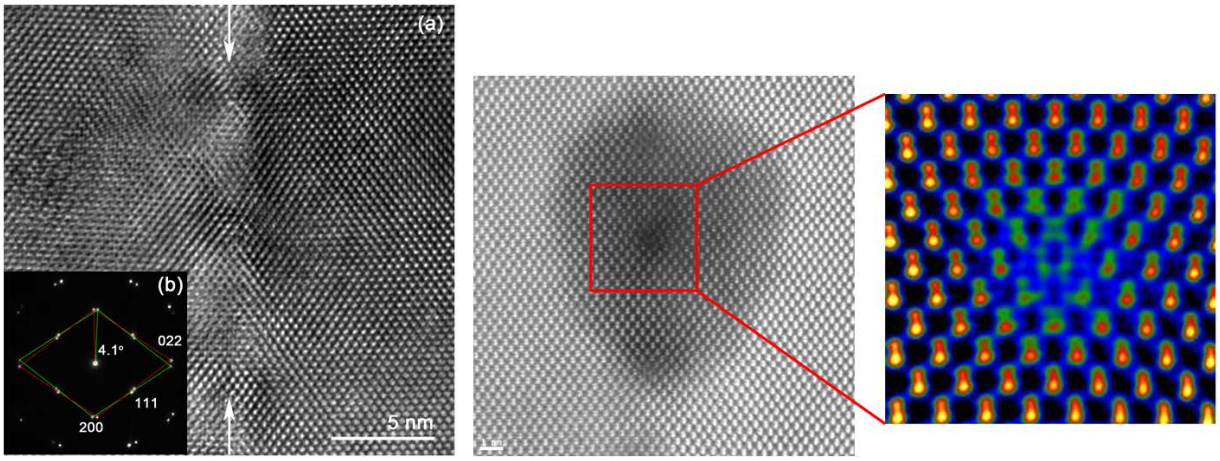

Figure 5: (a) Cross-sectional HREM image of the bonded CdTe (110) interface, showing the well bonded interface. (b) The diffraction pattern of the bonded pair indicates that the bonded pair is a (110) tilt boundary with a tilt angle of 4º. (c) Atomic-resolution Z-contrast image showing the atomic arrangement along the bonded interface and three isolated dislocation cores. (d) Magnified view of a dislocation core showing the atomic arrangement around the core.

The atomic-structure of low-angle tilt grain boundaries was studied using aberration-corrected Z-contrast imaging. We identified the structure of individual dislocation cores in 4° tilt grain boundaries with a (110) interfacial plane (Figure 5). While for low angle tilt grain boundaries the dislocations should only have an edge component (as shown in Figure 5c), in dislocations found in the CdTe bi-crystals are in general of mixed character having edge and screw components. Nevertheless, we find that pure edge dislocations are prevalent at the interface, which can be described as an intersection of two mixed 60° perfect dislocations on different {111} planes such that their anti-parallel screw components cancel. This vector can be obtained by two intersecting 60° perfect dislocations on different {111} planes making acute angle with respect to each other.

We further investigated the most prevalent dislocation and identified the Lomer-Cottrell (L-C), shown in Figure 6, and Hirth lock as the lowest elastic energy stable stair-rod dislocations. These dislocations are pure-edge and thus are likely candidates to be found at low angle tilt grain boundaries. In low angle grain boundaries, we expect the interface mismatch be completely accommodated by discrete arrays of edge dislocations with dislocation spacing approximately given by $D=|b|/\theta$; for tilt angle θ, burgers vector $|b|$. L-C and Hirth dislocation cores have well aligned atomic columns in the <110> direction and thus their electronic structure could be investigated as well. Furthermore, the core structure we found in the L-C dislocation was also found in a subset of structural units in {112} twin boundaries.

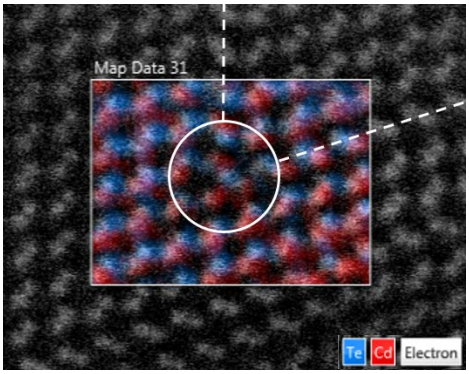

Figure 6: Atomic-column resolved XEDS map overlaid on top of the Z-contrast image in the <110> projection. L-C dislocation core (circled) is associated with the two dashed intrinsic stacking faults.

Subtask 3.2: Atomic-resolution characterization of high angle grain boundaries

Coherent {111} twin boundaries are the most common intra-grain planar defects in poly-crystalline CdTe. Figure 7 shows atomic-column resolved X-Ray spectrum image of a typical twin interface. We estimate on average 30 twinning boundaries per micrometer traversed in the direction normal to these interfaces, in both $CdCl_2$ treated and untreated poly-crystalline CdTe solar cell devices. The high density of twins in CdTe can be attributed to a rather low stacking fault energy, and coherent twins are seemingly benign in terms of lack of dangling bonds or the wrong Cd-Cd and Te-Te bonding. Nevertheless, the detrimental electronic properties associated with the twins could arise due to segregation of point defects as well as line dislocations driven by elastic interactions.

Using atomic-column resolved electron energy-loss spectroscopy (EELS), as well as XEDS, we found that twin boundaries in the samples without $CdCl_2$ treatment appear non-stoichiometric across and near the interface regions. There are alternating regions that appear Cd or Te deficient. Bulk areas of

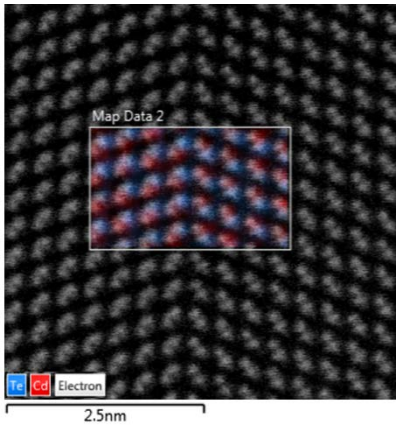

Figure 7: Atomic-resolution Z-contrast image of a coherent {111} twin boundary in CdTe along <110> viewing direction. Overlaid color-coded atomic-column resolved XEDS map shows polarity of Cd-Te dumbbells and its reversal across the twin interface.

untreated samples do not exhibit such noticeable variations. EELS and XEDS data indicate that samples after $CdCl_2$ treatment are stoichiometric across and around twin boundaries as well as in bulk. No chlorine is found near twins as well. Our first-principles DFT calculations (**Task 5**) initially focused on understanding these effects.

Task 4: First-principles modeling of grain boundary structural units

During the first 18 months, we have made significant progress in combining high-resolution STEM images and bi-crystal fabrication with first principles density functional theory (DFT) calculations. Early efforts focused on training a graduate student in DFT calculation methodology using the VASP code, testing of computational parameters, and some preliminary calculations on bulk CdTe. In parallel with these efforts, new capability was added with custom software to automate the creation of atomic structures and grain boundaries, as well as to analyze DFT output files, plot results, and submit follow-up calculations. DFT computation results were placed in a relational database structure for easy retrieval and future analysis. Furthermore, graphical user interfaces (GUIs) were created to generate grain boundaries directly from user input, or create random samples in a fully automated way. Great care was taken to reduce model structure sizes to repeating cells, and to properly cover the entire GB parameter space while invoking crystal symmetry.

Subtask 4.1: First-principles modeling of low-angle structural unit

Due to the prevalence of twin structures in the poly-crystalline CdTe solar-cell devices characterized by STEM imaging, we created models of and carried out extensive DFT calculations on <111> twin structures (Figure 8). Model structures were then created of all other bi-crystal interfaces currently fabricated and these structures are currently under analysis. A large series of grain boundaries with random orientations were also created computationally and are being investigated to guide future bi-crystal fabrication. Throughout the investigations of bulk, twin, and now general grain boundaries, we have focused on the study of energetics, strain, point defects, and electronic structure, in order to build a systematic understanding of the effects of extended defects on CdTe performance.

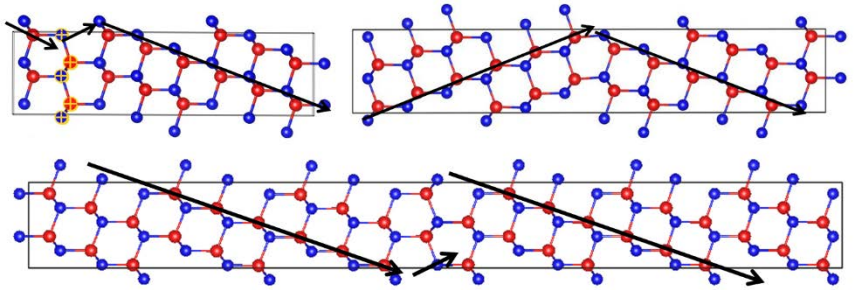

Figure 8: Examples of model twin structures. Top left: A^7B^1 stacking fault. Top right: A^6B^6 lamellar (repeating) twin. Bottom: $A^{19}B^1$ isolated stacking fault.

The <111> lamellar and isolated twins were created and relaxed, and their interfacial energies and local strain analyzed. We find very small interfacial energies for twins, consistent with their experimental prevalence. In order to understand the origin of the off-stoichiometry observed in STEM, we decorated twin models with point defects. For all intrinsic isolated point defects (vacancies, interstitials and anti-sites), formation energies near a twin is similar to in the bulk (Figure 9). We also investigated defect pair complexes, and our results show that in most

cases, a defect pair's binding is energetically less favorable when present along a twin, suggesting they are more difficult to form in proximity to a twin. Detailed analysis of the other GB structures is currently underway.

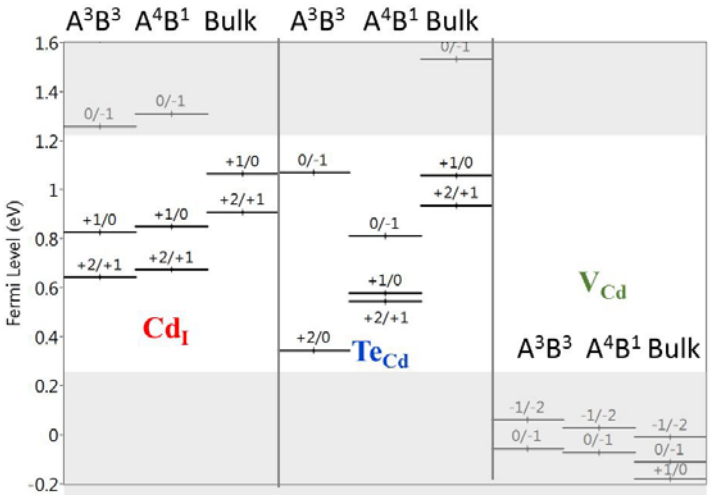

Figure 9: Defect energy transition levels for three point defects in three possible structures.

Subtask 4.2: Calculation of density of states for grain boundary structural units

Atomic structure models were created for all 8 of the bi-crystals prepared. Notation will follow the convention of (Twist Angle)[Grain 1 orientation][Grain 2 orientation] + (Translation), and any additional tilt angle is listed within grain 2 for convenience. The (60) [111][111] Σ3 twins show bulk-like density of states and are hence electrically benign. Analysis of the next 7 GBs is ongoing, with preliminary results mentioned here.

The (30)[111][111] bi-crystal structure conveniently exhibits a high degree of symmetry, allowing for the model structure to be significantly reduced in size. After relaxation, atoms near the boundary tend to pinch inwards in alternating patterns showing a near twin visible along the [110] direction (Figure 10a). As a result of this atomic misorientation, many additional states (Figure 10b) are created below the conduction band suggesting this interface is electrically active as a recombination center and possibly as an acceptor doping state. Such a structure however has a very high interfacial energy of 350 mJ/m², suggesting that it is more unstable and thus the model structure will need to be increased in size to be more representative.

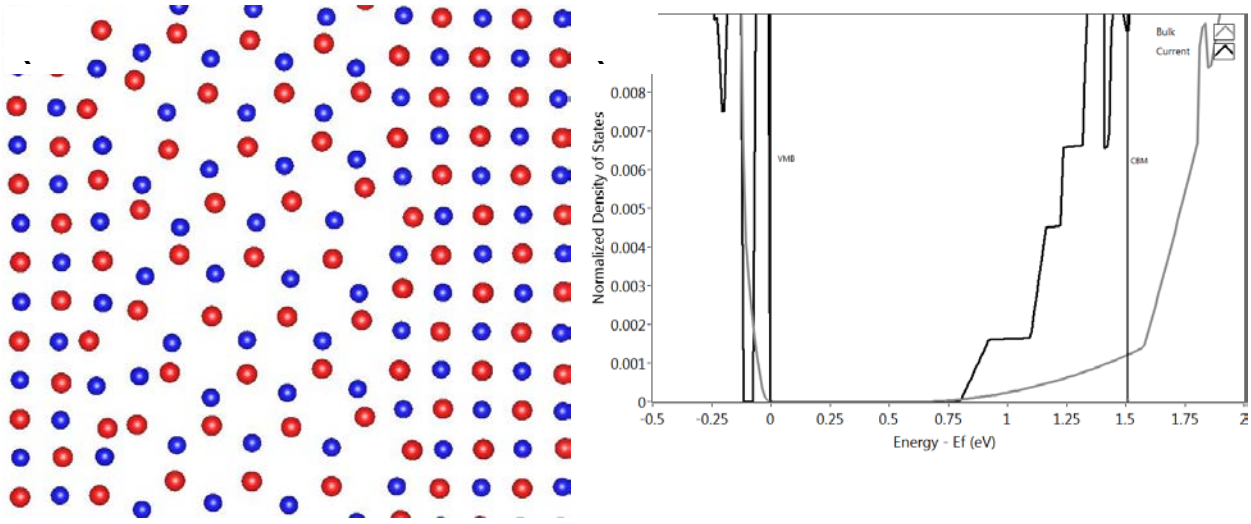

Figure 10: a) Preliminary relaxation of a (90)[110][110] grain boundary. b) Kohn-Sham density of states plot for bulk (grey) and the (90)[110][110] GB (black). Compared to the bulk, there may be enhanced DOS at the conduction band edge.

Deliverables and Go/No Go Criteria:

Deliverables Task 1 and Task 2: The successful fabrication of low angle tilt grain boundaries with a 4° misorientation angle and the deposition of p-type doped CdTe with a carrier concentration in excess of 10^{15} cm^{-3} have been demonstrated in Budget Period 1.

Deliverables Task 3: Atomic-resolution images, electron energy-loss spectra and energy-dispersive X-ray spectroscopy of individual dislocation cores and grain boundary structural units has been obtained in Budget Period 1. We have shown the effects of non-stoichiometric twin boundaries on the solar-cell performance and developed a model for several dislocation core structures that can occur in low and high angle grain boundaries.

Deliverable for Task 4: We have successfully developed a first-principle DFT model for grain boundaries, both high angle twist, coincident site lattice (CSL) and low angle grain boundaries. Using first-principles modeling, we have shown that specific point defect complexes can move the defect level away from mid-gap and thus act as a passivant.

Deliverables at 18 months: CdTe tilt grain boundary with 4° misorientation angle were successfully fabricated; atomic-resolution HAADF and EELS analysis of grain boundary structural units was achieved; and DFT model of dislocation core structure were developed.

Go/no-go criteria: Successful fabrication, analysis and modeling of low-angle grain boundary structure with 4° misorientation angle was achieved. Successful electronic transport measurements across the grain boundary demonstrating the effects of interfacial dislocation cores compared to single-crystal CdTe with the same doping concentration was demonstrated. We have successfully developed a model of most detrimental defects to electronic transport in twin boundaries and have proposed passivation mechanisms for those interfaces.

Budget Period 2:

Task 1: Fabrication of CdZnTe bi-crystals

The fabrication of CdTe grain bi-crystals continued in Budget Period 2. The focus of the bi-crystal synthesis was to reproduce grain boundary structures most likely found in poly-crystalline CdTe and in a zone-axis configuration that can be imaged using AC-STEM. Overall, we have fabricated 16 different grain boundary configurations, ranging from low angle twist to high-angle tile grain boundaries. In addition, we have also fabricated several CdTe/CdS hetero-interfaces to examine the structure and properties of an idealized p/n junction configuration.

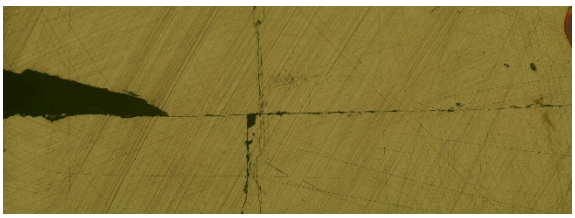

Figure 11: Optical micrograph of 2°(111) CdTe grain boundary.

Subtask 1.1: Fabricate low angle tilt grain boundaries

A 2° (111) tilt grain boundary was fabricated using two substrates, each with a respective miscut of 1°. Following the usual cleaning and alignment procedures, the grain boundary was formed using the high-vacuum wafer bonding approach. The resulting interface is shown in Figure 11, which indicates that there are cracks and voids at the grain boundary. An atomic-resolution STEM image of the well-bonded parts of the interface show it to be atomically abrupt (Figure 12). However, the interfacial structure appears different from any other grain boundary characterized to date, containing a single layer of atoms at the grain boundary plain. Using atomic-resolution XEDS and STEM imaging, this layer was identified to be Te while the two (111) CdTe wafers appear to be Cd terminated. These structures was confirmed using DFT modeling (see **Task 4**), and the current model suggests that the pre-bonding treatment left the two substrates

Table 2: Summary of bi-crystals bonded in Budget Period 2.

Wafer Plane	Bonded Orientation	Remarks
CdTe (100)	$[0\text{-}11]_1//[011]_2$	Well bonded
	2° tilt	Well bonded
	5° tilt	Well bonded
	8° tilt	Well bonded
CdTe (111)	$[0\text{-}11]_1//[0\text{-}11]_2$	Well bonded
	8° tilt	Well bonded
CdTe (110)	2° tilt	Well bonded
	5° tilt	Well bonded
	8° tilt	Well bonded
	$[1\text{-}1\text{-}2]_1//[\text{-}111]_2$	Well bonded
CdTe (311)	High angle	Well bonded
CdTe/CdS	5°	Well bonded

Te terminated. Upon bonding, the Te interfacial layer formed to compensate for the Cd, which now terminates the CdTe grains.

CdTe (110) 4° tilt bonded sample showed the Lomer dislocations at the bonded interface that can be separated into three distinct configurations. In order to see how the tilt angle will affect the configuration of dislocations, we fabricated new CdTe(110) bonded pair with 2° tilt. TEM images shows a clean interface and periodic dislocation cores. Diffraction pattern of the interface confirmed the tilt angle of 2°. The detailed atomic structure of the different dislocation cores was characterized using atomic-resolution STEM imaging and XEDS spectroscopy. **Task 2** discusses the identification of different structural units and dislocation core models.

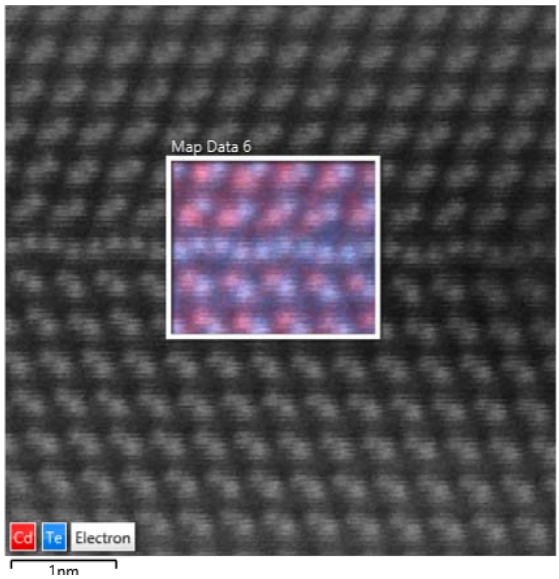

Figure 12: HAADF image and XEDS spectrum image of a 2° (111) CdTe grain boundary.

Subtask 1.2: Fabricate high angle tilt grain boundaries

We have fabricated CdTe (111) 180° twist boundaries shown in Figure 14a) and b) show well-bonded interface, and the diffraction pattern [Figure 14c)] shows the crystallographic relationship of two bonded pair. The investigation of the atomic arrangement at the interface is ongoing.

Figure 15 shows the bonded CdS/CdTe interface, which appears to be well bonded and without any amorphous layer. Crystallographic orientation across the bonded interface was not well controlled due to a slight miscut of the CdS crystal used. Diffraction analysis showed the miscut as much as about 5°. This kind of hetero-interface can now be used as a prototypical p-n junction to study the effects of interfacial defects on the local density of states and the overall solar cell performance.

EBIC is an ideal method to study the photovoltaic behavior of solar cells in short-circuit conditions. We used EBIC to detect the location of the homojunction in p-CdTe/n-CdS bonded sample. The SEM image in Figure 16a) shows the CdS/CdTe interface. An EBIC map was taken

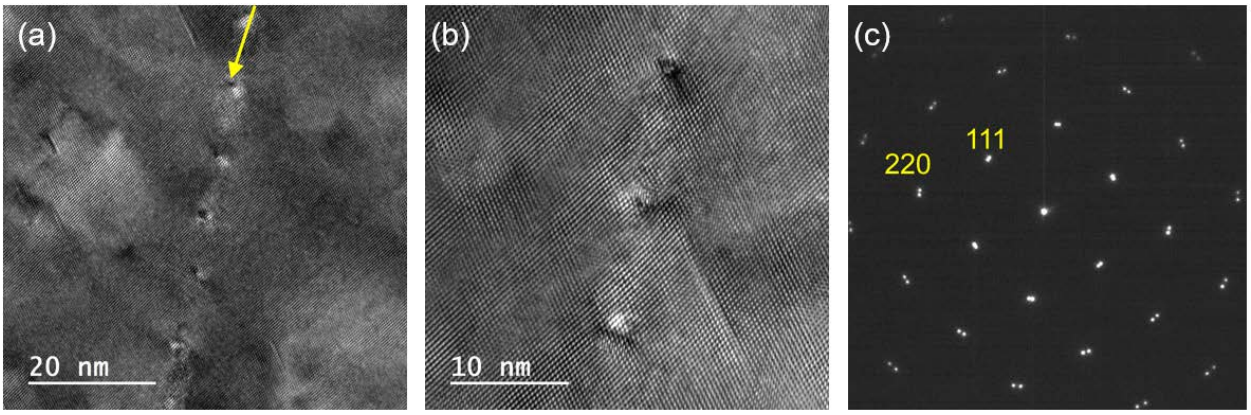

Figure 13: (a) Low magnification and (b) high magnification TEM images of CdTe (110) bonded interface. (d) Diffraction pattern (d) of the bonded interface in zone axis of [1-10], and shows tilt angle is 2.0°.

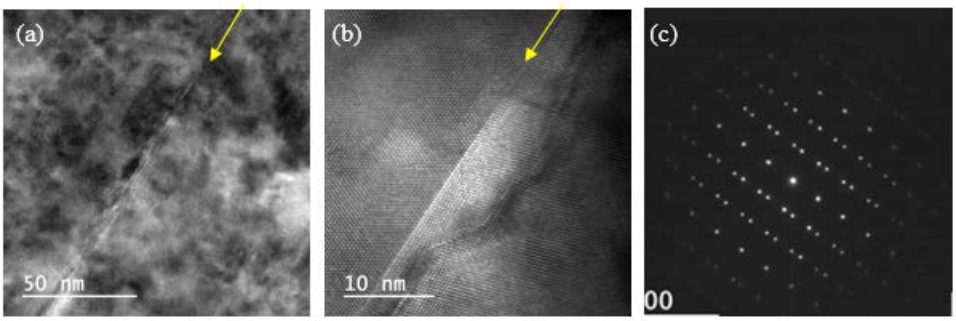

Figure 15: a) Low magnification and b) high magnification TEM images of CdTe (111) bonded interface. c) Diffraction pattern of the bonded interface at the zone axis of [0-11], and shows the twin structure.

simultaneously from the same area, as shown in Figure 16b). For cross-sectional EBIC, the EBIC current maximum typically occurs at the region with the highest internal electric field as defined by the p-n junction space charge region (SCR) and decays exponentially away from the p-n junction SCR, as shown in the overlapped image (Figure 16c)) of SEM and EBIC. Two line profiles of the EBIC current and SEM contrast across the CdS/CdTe interface can be seen in Figure 16d). In this case, the position of the p-n junction has been pushed inside the CdTe, which is likely caused by minority carrier diffusion.

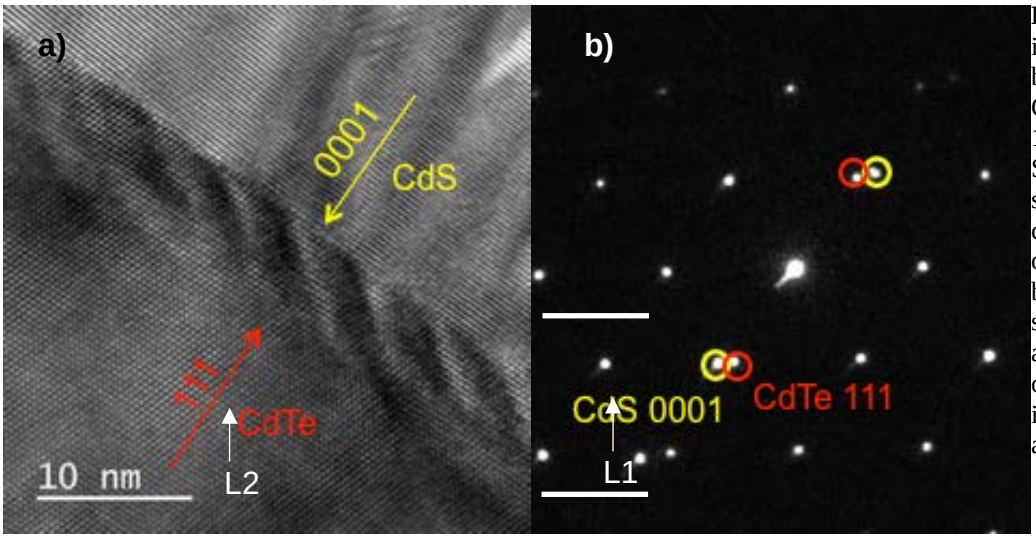

Figure 14: HREM image of the bonded CdS(0001)/CdTe(111) interface. (b) SAED pattern shows the crystallographic orientation of the bonded pair. A slight miscut of about 5 ° was observed, resulting in Moire fringes along the interface.

Subtask 1.3: Fabricate doped tilt grain boundaries

Several low angle tilt grain boundaries were passivated or doped using $CdCl_2$ exposure, Cd overpressure treatments or hydrogen exposure. The treated grain boundaries, as well as the corresponding bulk CdTe single-crystal samples were characterized using AC-STEM and TRPL Figure 17 shows an optical image of various low angle tils grain boundary samples prior to $CdCl_2$ or Cd overpressure exposure.

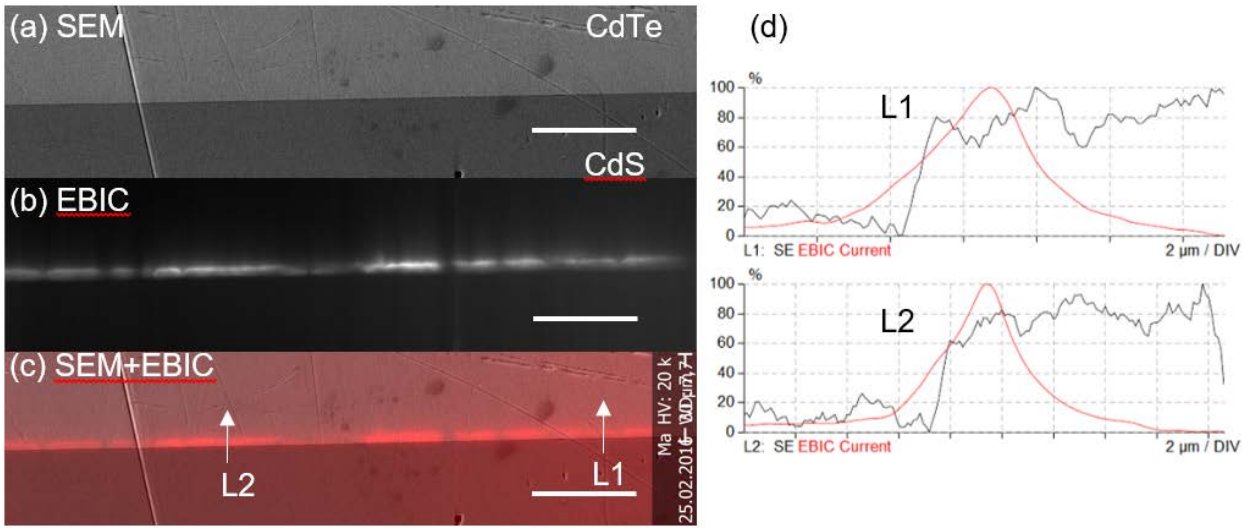

Figure 16: a) SEM, b) EBIC, and c) overlapped image of CdS(001)/CdTe(111) bonded pair. Scale bar, 10 um. d) SEM and EBIC line profile.

Task 2: Synthesis of p-type doped CdTe thin films

In Budget Period 2, the focus of this task was on depositing highly-doped CdTe thin films using either N or As as a *p*-type dopant.

Subtask 2.2: Synthesize doped CdTe on high angle grain boundary substrates

It is well known that improving the open-circuit voltage (V_{oc}) is crucial to increasing the efficiency of CdTe thin films solar cells. Fundamentally, a higher carrier concentration and a longer minority carrier lifetimes are necessary to achieve this task. There are, however, practical challenges to achieving hole carrier density $>10^{15}$ cm^{-3}. Nitrogen and Arsenic dopants, acting as shallow acceptor states, were investigated as an alternative to the conventional Cu doping of CdTe films. To investigate incorporation and activation of the dopants and correlate to the resulting atomic-scale crystal quality in a reproducible and well-controlled way, a single-crystal Molecular Beam Epitaxy (MBE) grown CdTe on Si (211) substrates were used. As reported for Budget Period 1, thin film synthesis of p-type doped CdTe with a carrier concentration exceeding $4x10^{15}$ cm^{-3} has been achieved using As. The crystal quality appears to decrease as a function of the *p*-type doping using As, which might negatively affect the minority carrier lifetimes. Using N as a p-type dopant

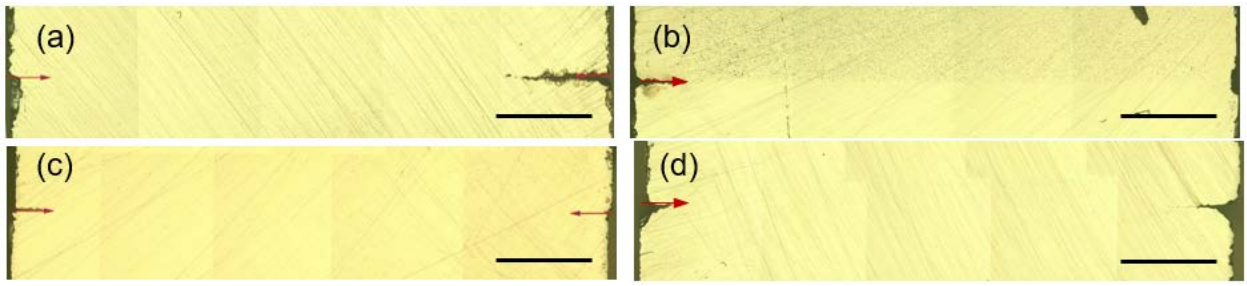

Figure 17: Optical images of CdTe (100) **(a)** 0°, **(b)** 2.6°, **(c)** 2.8 and (d) 7.8 tilt boundaries. Red arrows showed the bonded interfaces. Scar bar 1mm.

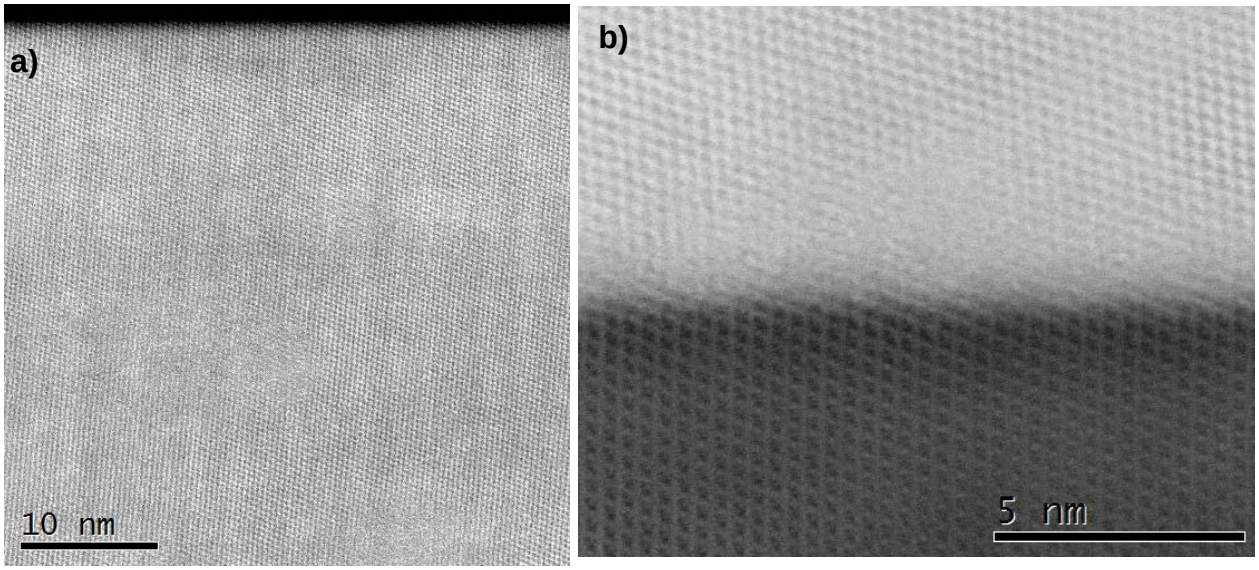

Figure 18: a) High angle annular dark field (HAADF) image of a CdTe thin film near the Si substrate (dark). b) Annular bright field (ABF) image of CdTe(110)-Si(110) interface.

appears to be possible with carrier concentrations similar to those reported for As-doped CdTe thin films. Moreover, the crystal quality does not decrease as the N-doping concentration is increased.

Figure 18a) shows a low-magnification overview of the CdTe thin film in the (110) orientation doped with Nitrogen. The Si substrate in this high angle annular dark field (HAADF) image appears dark at the top. Since Si atoms have much lower atomic number, the high angle scattering signal collected by the detector is dominated by Cd and Te atomic columns. The image demonstrates a general trend observed near CdTe-Si interface, namely that the interface is atomically smooth and of high crystal quality, with very few defects and dislocations. Figure 18b) shows the interface up close, in an annular bright field (ABF) image with both Si substrate (top bright), and CdTe (dark), visible simultaneously.

The overall CdTe film thickness is 10 µm, with the bottom 5 µm being undoped CdTe and only the top 5 µm being doped with N. In the N-doped CdTe film, a few dislocations start appearing as shown in Figure 19. However, the dislocation density is still rather low, without any observable

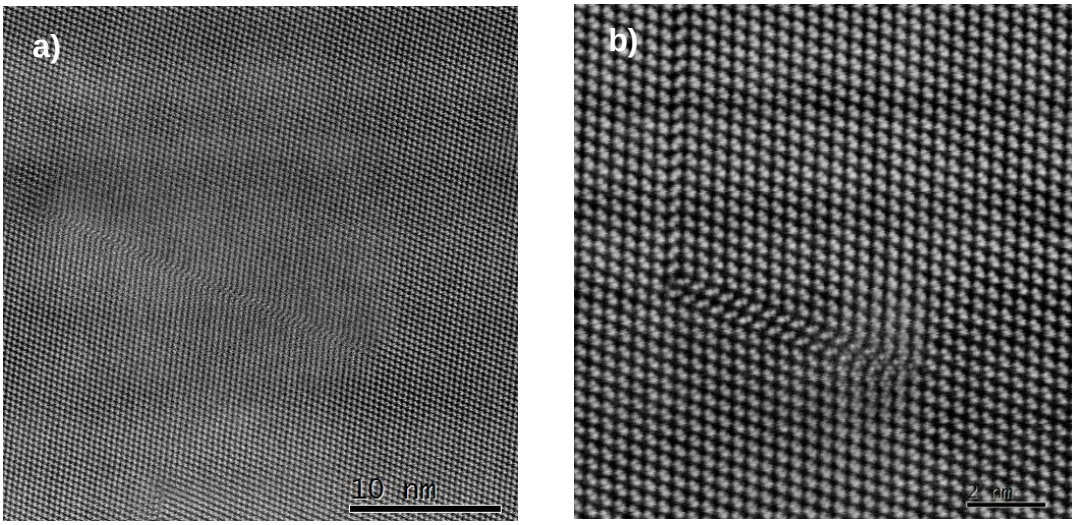

Figure 19: a) N-doped CdTe film showing a dislocation, b) magnified view of the dislocation.

large defect complexes or treading dislocations. Figure 19a) and b) show some of the typical dislocations that were found. Figure 19a) shows a dissociated dislocation with an extrinsic stacking fault, roughly 20 nm in size. Most of the dislocations observed were straight dislocations 10 – 20 nm in length, with single or double stacking faults. Few were found forming dislocation junctions, as shown in Figure 19b).

Atomic-scale imaging of Arsenic doped CdTe films indicate that the resulting crystal quality is similar to that of the Nitrogen doped CdTe films, at least on the local atomic scale. Very few dislocations were present as different areas of the As-doped film were sampled, with many large regions appearing completely free of dislocations. A representative HAADF image of As doped CdTe is shown in Figure 20.

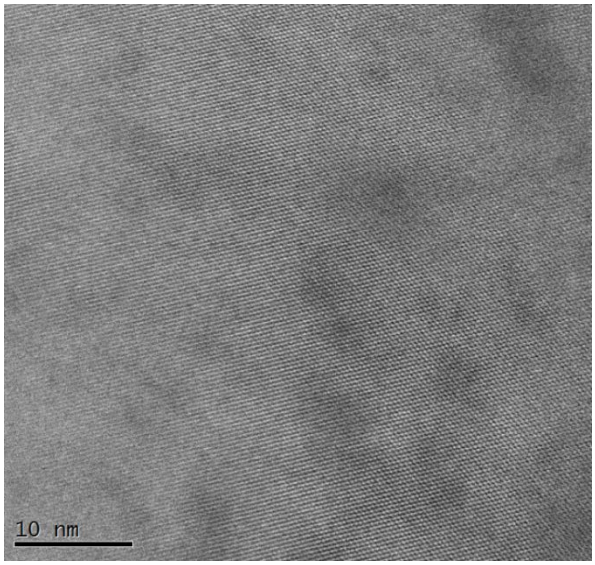

Figure 20: HAADF image of As-doped CdTe.

Subtask 2.3: Synthesize grain boundary doped CdTe thin films tilt grain boundary substrates

Since the minority carrier lifetimes, as measured by TRPL (see **Task 3**), were significantly shorter than expected in both the CdTe thin films as well as the bi-crystal samples, the PI focused on treated the CdTe samples with either $CdCl_2$, a Cd overpressure environment or H incorporation. The $CdCl_2$ treatment usually employed for poly-crystalline CdTe devices is performed at temperature above or close to the bonding temperature of the PI's bi-crystal samples. The PIs performed extensive modeling of the Cl diffusion in CdTe for different temperatures and exposure times. Table 1 shows a summary of the treatment conditions used for both single-crystal and bi-crystal samples. The results of the TRPL measurements will be reported in the following section.

Table 3: Summary of treatments for CdTe single crystals.

Single-crystal sample number	**Treatment**
2405	Hydrogen treatment at room temperature
2406	Cd overpressure anneal at 400 °C for 24 h
2408	$CdCl_2$ anneal at 350 °C
2409	$CdCl_2$ anneal at 400 °C

Task 3: Atomic-scale characterization of CdTe grain boundaries

A CdTe [1-10]/(110) 4.8° tilt grain boundary was fabricated and characterized using AC-STEM imaging (see Figure 21). Electron diffraction patterns and high-resolution transmission electron microscopy images demonstrate the crystallographic orientation relationship and confirm

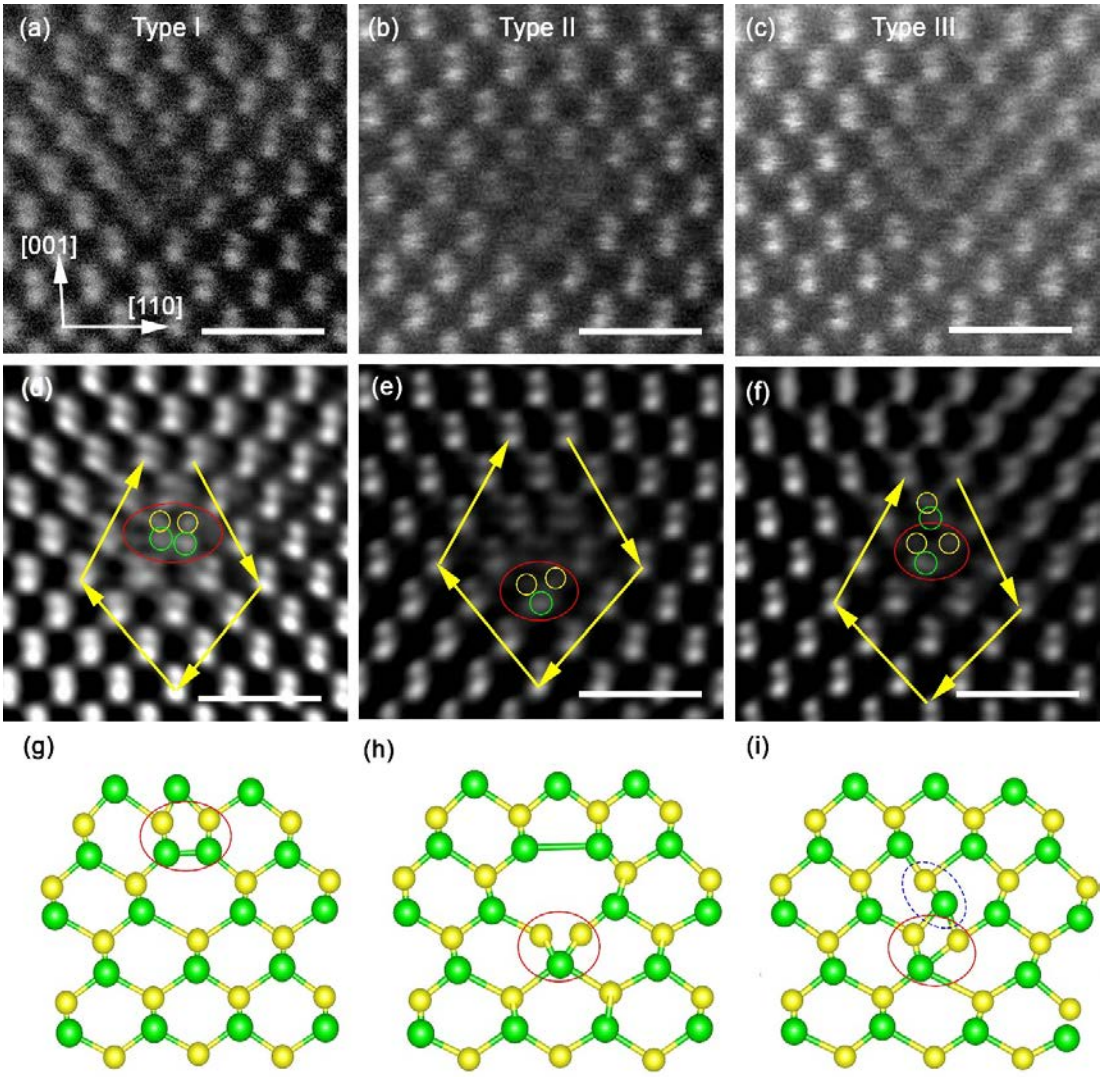

Figure 21: Dislocation core structures of the bonded CdTe [1-10]/(110) 4.8° tilt boundary. (a)-(c), Experimental HAADF-STEM images of three types of dislocation cores observed along the boundary. (d)-(f), Fourier filtered images of (a)-(c) show atomic arrangements at these dislocation cores. Yellow lines indicate the Burgers circuit. (g)-(i) Atomic models of the core structures for (d)-(f), respectively. Scale bar = 1nm. Viewing direction [1-10].

the grain boundary misorientation angle. It should be noted here that the intended misorientation angle was 4°, but the CdTe substrates were polished to a slightly higher angle, resulting in a final misorientation angle of 4.8°. High-angle annular dark-field (HAADF) scanning transmission electron microscopy (STEM) images show three kinds of 90° dislocation cores (Figure 21), a Frank partial dislocation dissociated to an intrinsic stacking fault with a 30° Shockley partial dislocation, and two 60° dislocation cores. Local strain maps shoes a very localized strain field around the different kinds of dislocation cores that are formed in the tilt grain boundary. Detailed analysis of the dislocation core structures and the resulting density of states was performed in **Task 4**.

In collaboration with Dr. Edward Barnard at Lawrence Berkeley National Laboratory (LBNL), the we also measured the minority carrier life time of CdTe bulk and the bonded grain boundaries as a function of misorientation angle using time-resolved photoluminescence (TRPL).

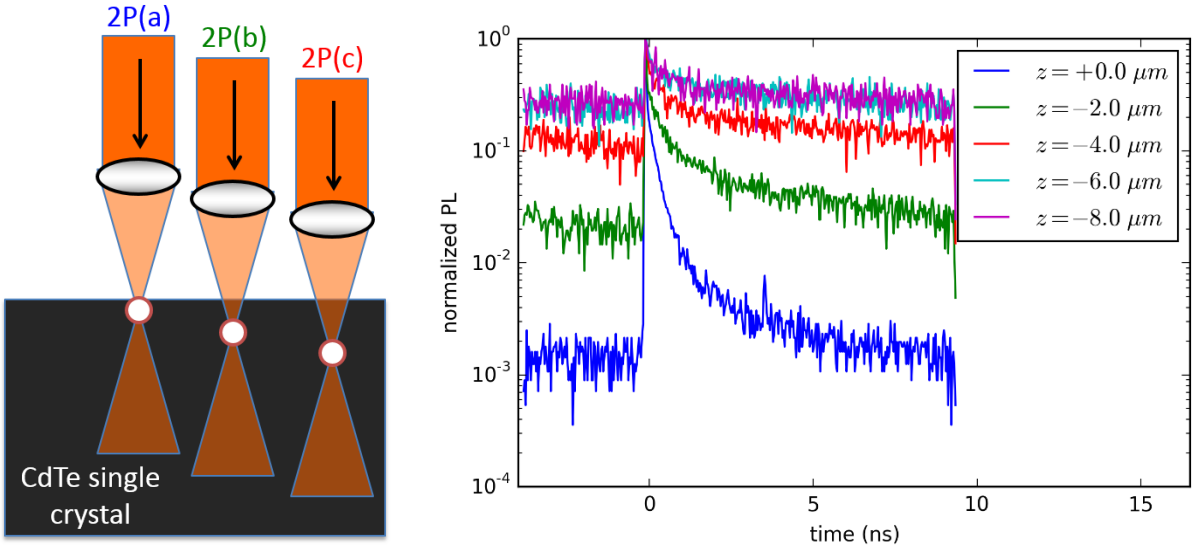

Figure 22: Schematic drawing of the laser probe position with respect to the CdTe single crystal sample (left); PL signal for different probe depth.

The non-linear absorption of sub-band gap photons allows one to control depth of the excitation volume in CdTe and thus to de-couple surface recombination from bulk recombination processes. Traditional one-photon absorption techniques are unable to do this as optical absorption typically follows Beer's law attenuation and are thus only surface sensitive. This is particularly important for studying grain boundaries since recombination velocity of the interfaces can be comparable to the top surface recombination making it difficult to separate these two contributions. In addition, sample stage setup in the LBNL microscope provides a unique ability to construct sub-micrometer resolution three-dimensional spatial maps of recombination processes using two-photon excitation.

Initial experiments were conducted on CdTe material used for the bi-crystal formation. Figure 22 shows a schematic of the laser position within the CdTe crystal, as well as the measured PL signal. The lifetime traces were fitted with a bi-exponential curve at each depth of the form

$$PL(t) = a_0 e^{-\frac{t}{\tau_0}} + a_1 e^{-\frac{t}{\tau_1}}, \qquad (1)$$

where τ_1 and τ_2 are two fitting parameters corresponding to the surface and bulk lifetime; a_0 and a_1 are the relative weights of the two lifetimes. It was found that the shortest lifetime is measured at the sample surface due to high surface recombination, as expected. The surface lifetime for the samples measured here is approximately 0.3 ns. The bulk lifetime increases to larger than 60 ns in the sub-surface bulk CdTe.

Figure 23a) shows high-angle annular dark field image of a symmetrical tilt bi-crystal with (111) interface plane and 5° tilt. The interface can be seen as composed of evenly spaced (~4 nm) 60° mixed character edge/screw dislocations. The dislocations are due to an extra (111) plane terminated at the CdTe glide planes and thus having extra Cd column at the cores. Cross-sectional photoluminescence intensity map (Figure 23b) of the same interface clearly shows reduced light emission from and near the bi-crystal interface region. Low photoluminescence efficiency usually indicates increased non-radiative recombination. The underlying effects for low emission can be better understood by looking at the transient signal decays. The decay signals were fit with a bi-

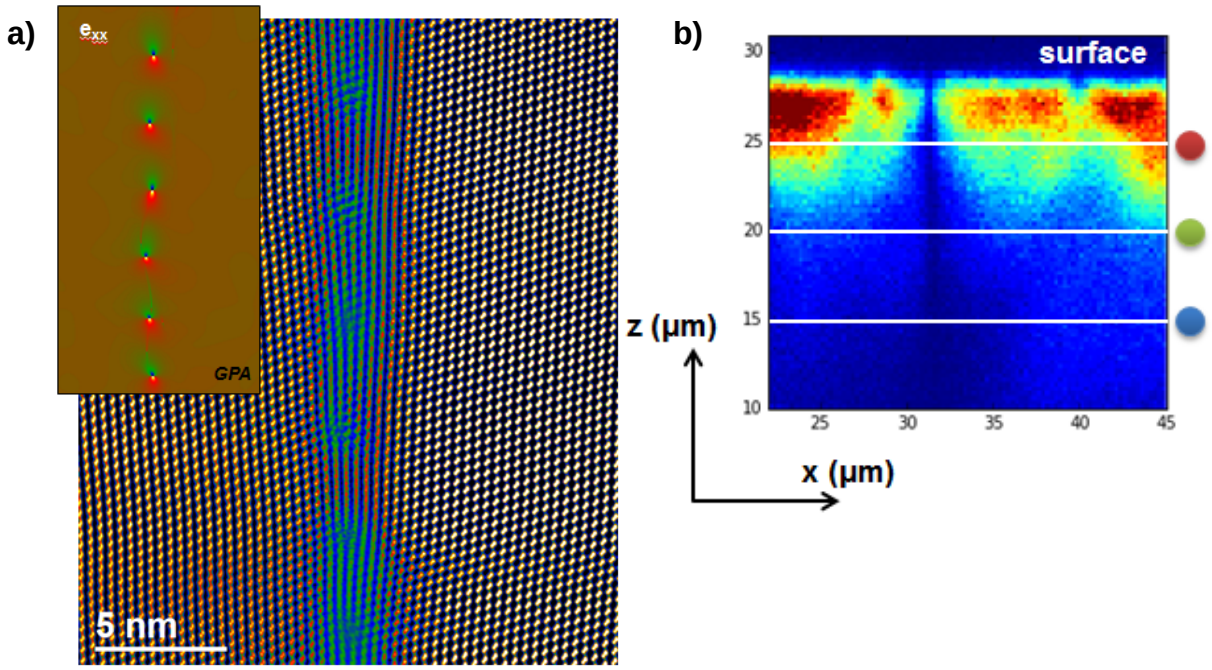

Figure 23: a) HAADF image of (111) 5° bi-crystal interface region and the dislocation strain fields; b) cross-sectional photoluminescence intensity map of the (111) 5° bi-crystal.

exponential function and are shown in Figure 24. In Figure 24a) three different nominal depths 25 μm (red), 20 μm (green) and 15 μm (blue) were profiled. τ_0 and τ_1 correspond to the shorter and longer lifetime constants (ns) of the fit, respectively. Figure 24b) shows corresponding 2-D lifetime maps of the interface. The overall short lifetimes are expected from the bi-crystals since they are non-post growth treated and likely contain high density of bulk Cd vacancies which are expected to act as recombination centers.

However, looking at the relative changes in lifetime profiles across interface it is clear that there is a pronounced dip for τ_0 right at the interface and an extended decay, over ~5 μm, in τ_1. τ_0 corresponds to an initial decay of PL intensity, it's weight is more pronounced right at the interface, while τ_1 has the dominant weight in the bi-exponential fit further away from the interface.

Surface recombination velocity is the analog to bulk SRH recombination to quantify the rate of non-radiative charge carrier recombination. In general, it is proportional to the areal density of mid-gap level states at the interface and electron/hole capture cross-sections of these centers. In addition, the occupancy of the interface states will depend on position of the bulk Fermi level relative to the interface neutrality level. This in turn determines whether the interface accumulates electrons or holes in equilibrium with the bulk and the width of space charge region (SCR) that can be established around the grain boundary. Thus, upon creation of electron-hole pairs by laser pulse, the carriers will diffuse due to density gradients and may also drift towards/away from the interface due to the band-bending at SCR which will affect surface recombination rate. Low τ_0 right at the interface indicates that there is pronounced surface recombination velocity. The extended region of decreasing τ_1 towards the interface suggests that there is an additional carrier dynamics taking place after the laser excitation which causes the low lifetimes. In particular, it is possible that the carriers diffuse towards the grain boundary where they rapidly recombine with interface defects. The extent of decreasing τ_1 is close to the diffusion length. In addition, since the

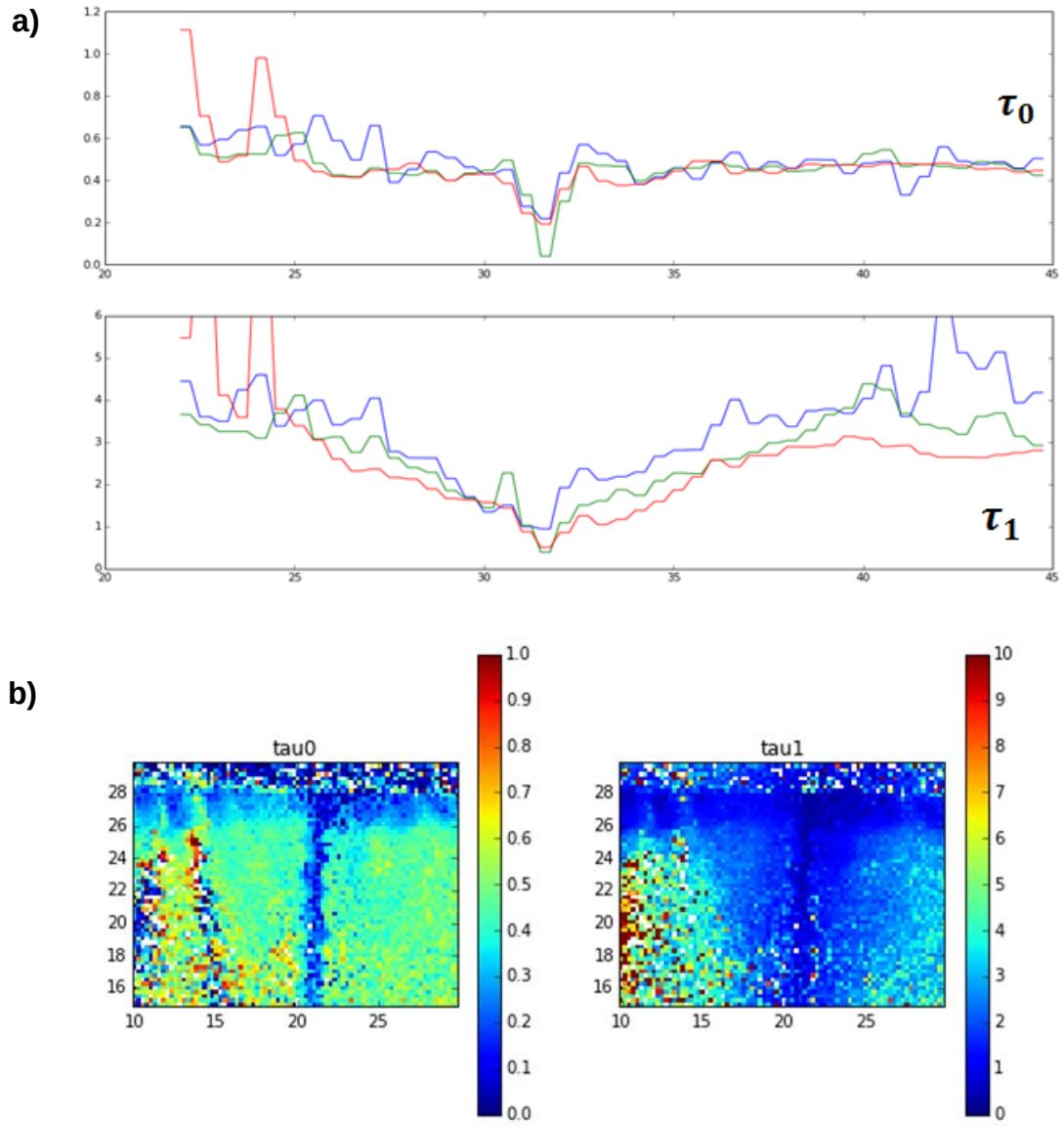

Figure 24: a) Lifetime profiles across the interface located at x~32 µm. Horizontal axis shows position in µm, vertical –time in ns.b) 2-D lifetimes maps of the interface. Color scale in ns, x-z positions in µm.

intrinsic doping levels of the bi-crystal (~10^{12} cm^{-3}) is rather low there is a possibility to establish very wide depletion region if interface state density is high compared to the background doping.

DFT modeling of the interface can indicate position of the mid-gap states, their charge levels and possibility of establishing SCR. The areal density of these states can then be estimated based on number of interfacial dislocation cores from the images. Additional experiments could also be performed by varying applied bias across the interface. This will change bulk Fermi level and thus occupancy of the interface states which in turn will change width of the SCR. Repeated TRPL measurements with an applied bias could provide an estimate of the depletion width/barrier height as well as the grain boundary interface charge density.

We also performed additional electron energy low-loss spectroscopy (EELS) across the (111) 2° tilt grain boundary (see Figure 12). The resulting spectra (Figure 25) show a pronounced

shift in the low-loss region as one scans across the interface. Given that the low-loss signal is highly delocalized (~5-10 nm) the high intensity of the peak appearing in the spectra and originating from the interface indicate dramatic rearrangement of the bulk valence electrons. It could also suggest that the interface is transformed into metallic two-dimensional layer sandwiched between bulk CdTe. A combination of DFT calculations and high energy resolution low-loss spectra taken with monochromated electron microscope should elucidate nature of this interface.

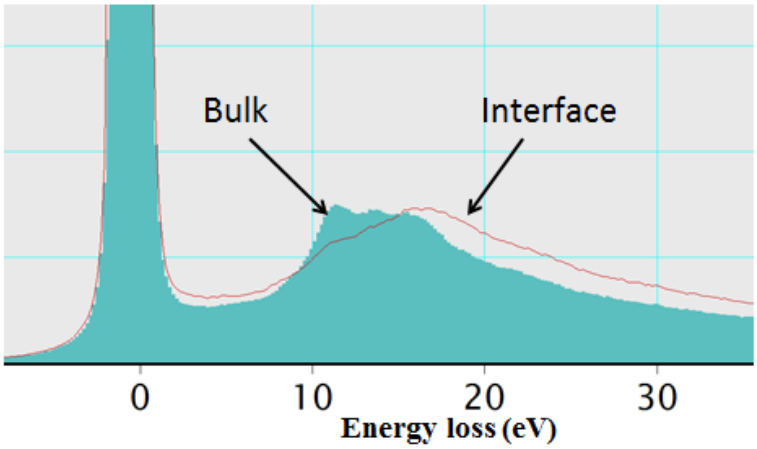

Figure 25: Electron energy low-loss region of the spectra. Shift of the bulk peaks versus spectra from the interface (red line).

We also continued studying effects of $CdCl_2$, as well Cd-overpressure and H treatments on the bicrystal grain boundaries. In the previous quarter, we coordinated $CdCl_2$ treatment of (111) 5 degree tilt bi-crystal. The sample was subjected to the treatment at 350 °C for 30 minutes. This temperature was chosen to be below the wafer bonding temperature of 400 °C to maintain integrity. Subsequent lifetime measurements performed at LBNL sample showed bulk lifetimes lower by almost a factor of 10 throughout the wafer as compared to results before the treatment on this same

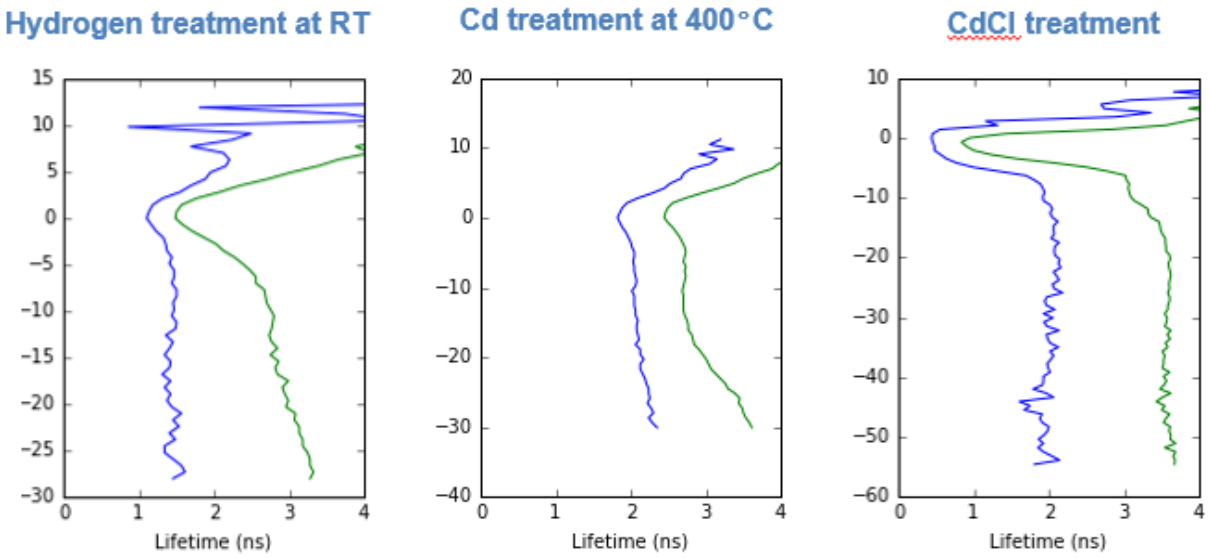

Figure 26: TRPL minority carrier lifetime measurements for single crystal wafers treated under different conditions. The x-axis displays the carrier life-times in ns, while the y-axis is the sample depth, where 0 corresponds to the surface. The blue curve shows the short lifetime and the green the longer life-time components of the exponential fits.

sample. Lifetime measurements of the grain boundary region was unreliable since it may had been easily obscured due to very low bulk lifetimes.

We suspected that the annealing may have created additional bulk Cd vacancy defects. In order to test the hypothesis we subjected the sample to Cd overpressure treatment. The Cd anneal was done at 350 °C for 24 hours. Subsequent measurements at LBNL indicated slight improvement recovering lifetimes in the bulk close to original values. This took place mostly in the first 5-10 micrometers of the sample.

We have been further carrying various treatment experiments. Cd anneal has been performed on a new CdTe wafer, at 400 °C for 24 hours. Another piece from the same wafer has also been treated with $CdCl_2$ at 400° C, while a separate sample was treated with hydrogen at room temperature to test the effect of hydrogen incorporation on the lifetimes.

Figure 26 shows a summary of the single crystal TRPL lifetime measurements for wafers exposed to different treatment conditions. As can be seen from Figure 26, the bulk lifetime appears to be limited to 3-4 ns, which is substantially shorted than we expected for bulk CdTe. The actual bi-crystal sample appears to have recovered to the bulk lifetimes prior to the $CdCl_2$ treatment while the grain boundary lifetimes are still one order of magnitude shorted than in the bulk.

Task 4: First-principles modeling of grain boundary structural units

We completed the first principles calculations of defect pairs at twin boundaries, built the Grain Boundary Genie code to create arbitrary atomistic models of grain boundaries (GBs), and performed atomistic and first principles calculations of fabricated bi-crystals. Additionally, we perfectly interfaced STEM images acquired at fabricated CdTe bicrystal interfaces with atomistic models. We particularly focused on fabricated 4.8º (110)||(110) and 2º (111)||(111) grain boundaries and revealed that both grain boundaries are detrimental for solar cell efficiency. Finally, we constructed three-dimensional atomic model of a single-layer Te, tellurene, formed at 2º (111)||(111), which may have unusual electronic properties.

Point defect and point defect pair structures along twin boundaries were exhaustively studied using DFT calculations of twin boundary models of different periodicity. The energetics of some point defects, such as Te interstitials, are drastically different when present along a twin boundary compared to in bulk, partly due to a difference in symmetry. The defect levels are obtained from charged defect calculations, and for some defects (Cd_I, Te_{Cd}, Te_I) were found to move towards the Fermi level when present near a twin (compared to the same defects in bulk), which is detrimental to performance. The reduced likelihood of charge-compensating defects to bind at twins further increases the negative effects of twin boundaries.

Our exhaustive study of point defects and defect pairs at or near twin boundaries – the most prevalent grain boundaries in poly-CdTe – reveal that despite a lack of midgap states in the density of states in the absence of point defects, twins could nonetheless be mildly detrimental to device performance due to the movement of charge transition levels towards the midgap induced by point defects.

We developed a custom code (Grain Boundary Genie) to generate atomistic models of GBs of arbitrary crystal planes, twists, and tilts. The Grain Boundary Genie code builds fully periodic models in three dimensions based on user specification of maximum number of atoms in the model. It also allows specification of STEM viewing angles. This code allows for the modeling of arbitrary grain boundaries using empirical potentials and density functional theory (DFT).

Subtask 4.1: First-principles modeling of low-angle structural unit and Subtask 4.2: Calculation of density of states for grain boundary structural units

We generated atomic structures of various high angle symmetric/asymmetric tilt (ATGB) and twist (TwGB) grain boundaries of CdTe and evaluate the interfacial energies using the Stillinger Weber and bond order potentials. We find that ATGBs have a larger range of interfacial energies (~0.1 – 1.5 J/m^2) compared to TwGBs, which tend to have moderate to high interfacial energies (0.6 – 1.4 J/m^2). Several representative GBs of each type with reasonable interfacial energies were selected and the electronic structure was computed using DFT. Most of the selected ATGBs and TwGBs showed formation of midgap states due to the dangling bonds at the disordered grain boundary interface, but the density of midgap states vary significantly among the different ATGBs with some having almost no midgap states.

We have focused our detailed modeling efforts on fabricated bi-crystal [1-10][110] 4.8° tilt GB. Based on the experimental data shown in Figure 21, using a combination of image analysis, empirical potential modeling, and DFT calculations, we have obtained three-dimensional structural models of three types of dislocation cores at the GB. Types I and II were modeled using a dislocation dipole model, whereas Type III consists of a stacking fault terminated with two dislocation cores. Because of the requirement of periodic boundary conditions, combined with the small angle of the tilt, these structural models are relatively large, consisting of several hundred to over a thousand atoms. Figure 29a shows that the model corresponds exactly to the STEM images. The electronic structure of the dislocations is analyzed in terms of density of states (DOS). We integrate the projected DOS of atoms in a cylindrical volume around the dislocation core, and compare the result with the DOS of the bulk reference area, which is selected from the same simulation cell far from the dislocation cores. Figure 29b shows the integrated DOS around Type I and II dislocation cores, respectively, near the Fermi level, compared to bulk reference in the simulation cell. Figure 29b shows that the dislocation cores give rise to additional electronic states within the bulk band gap. While the bulk-like region of the simulation cell may not reproduce bulk CdTe exactly due to the residual strain field created by the dislocation cores, the bulk-like region exhibits a gap similar to the Kohn-Sham band gap (~0.6 eV) of bulk CdTe. The bulk-like region also shows negligible DOS within a gap of about 1.3 eV, similar to bulk CdTe. The DOS shows different characters for the two different cores. The differing characters are also revealed in the

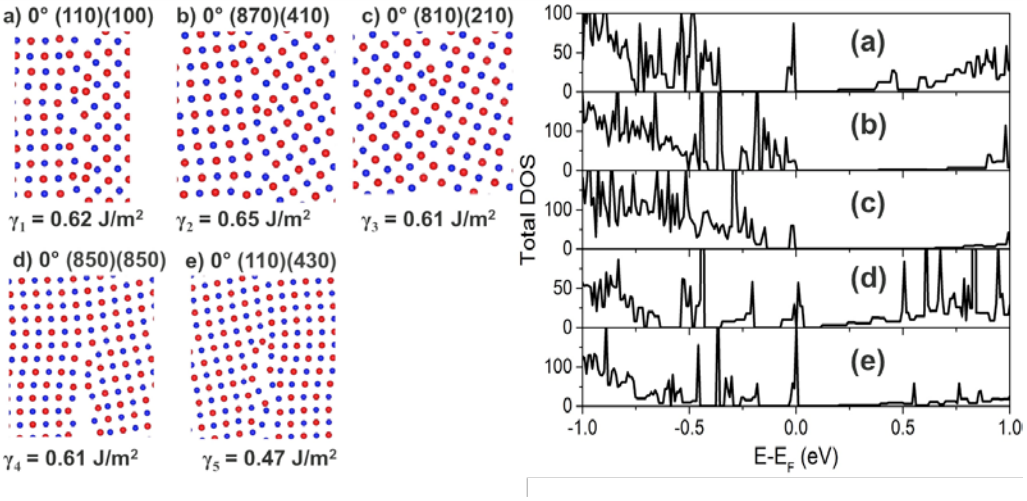

Figure 27: Atomic structures (left) and density of states (right) of a) ATGB-1 0°(110)||(100) (b) ATGB-2 0°(870)||(410), c) ATGB-3 0°(810)||(210), d) ATGB-4 0°(110)||(430), and e) ATGB-5 0°(430)||(110).

Bader charges (not shown) and average electrostatic potentials (Figure 29c), which show that core I exhibits strong electron repulsion (hole attraction) whereas core II moderate exhibits hole repulsion (electron attraction). As a result of change in the coordination, both Te and Cd atoms in the dislocation core had smaller magnitude of Bader charges than the bulk. The deviation of the Bader charges at the dislocation core compared to the bulk values is attributable to the change in coordination, which can give rise to the formation of additional states in the band gap.

A single layer of Te atoms was observed with STEM at the 2º (111)||(111) CdTe grain boundary as shown in Figure 12. DFT calculations were used to elucidate the 3D atomic structure of the single Te layer, namely "tellurene". We used the atomistic models produced from Grain Boundary Genie as a start, and performed DFT relaxations to produce the atomistic model, showing an excellent match. The simulated HAADF STEM image using Kirkland's multislice program also shows an excellent match with the actual image in terms of column positions of the interfacial atoms and bulk CdTe regions, as well as column contrast.

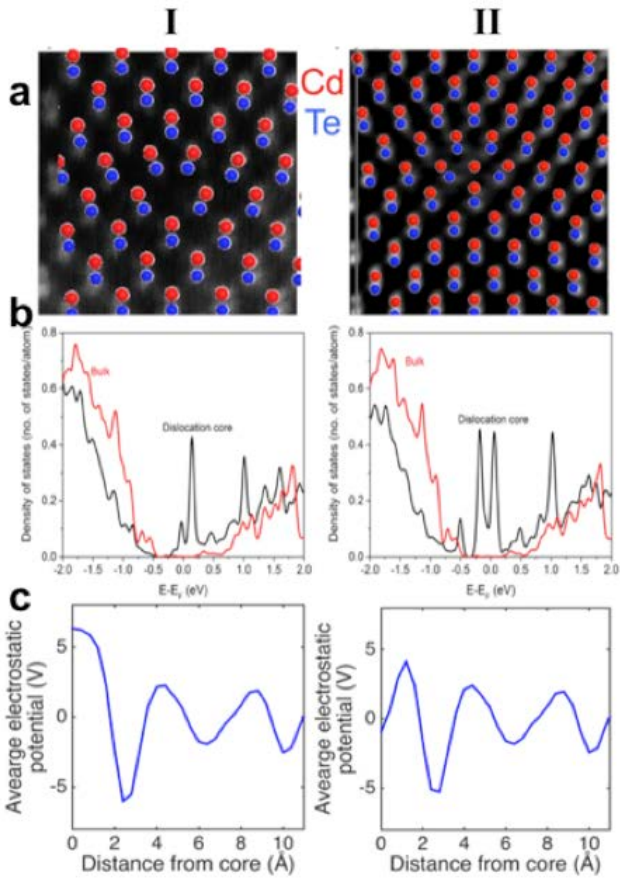

Figure 28: Two types of dislocation cores at the [1-10][110] 4.8° tilt bicrystal. (a) Atomistic model overlaid on STEM image; (b) density of states near (black) vs. away from (red) the cores; (c) average electrostatic potential as function of distance from the core.

Task 5: Passivation of CdTe grain boundaries

We have performed a computational survey of the GB parameter space in order to identify representative GB structures that require different levels of passivation. Using the Grain Boundary Genie code, the PIs produced atomistic structures of GBs with full periodic boundary conditions within the smallest number of atoms possible. Using the calibrated Stillinger-Weber and Bond order empirical potentials, the PIs evaluated several hundred GB structures based on their interfacial energies. Several main types of grain boundaries, including coincident site lattice (10), those near the McKenzie peak (53) and asymmetric tilt grain boundaries (854) were investigated. Based on the interfacial energies from these 917 GB structures, the PIs selected 11 to perform DFT calculations and from those, several structures for further bi-crystal fabrication.

In order to perform a systematic study of GB electronic properties and passivation strategies, we generated over 900 GB structures and performed atomistic modeling to down-select representative samples. On nine of these GB structures, including five asymmetric tilt (ATGB) and four twist GBs (TwGB), we performed DFT calculations including DOS and average

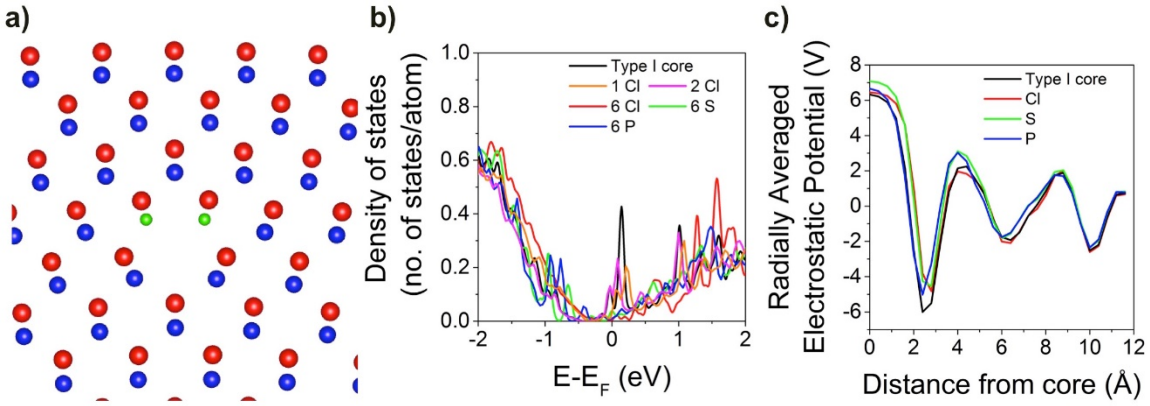

Figure 29: a) Atomic structure of Type I dislocation core at 4.8º (110)||(110) grain boundary. b) Radially integrated density of states (DOS) around dislocation core doped with 1 Cl, 2 Cl 6 Cl, 6 S and 6 P atoms. c) Radially averaged electrostatic potential profile with different dopants.

electrostatic potentials. We found that the ATGBs sampled tend to exhibit electron repulsion (hole attraction) at the GB, whereas the TwGBs can have either electron or hole repulsion.

Subtask 5.1: Identify stable grain boundary passivants

We investigated the effect of doping on the electronic structure of Type I dislocation core, which has an atomic structure shown in Figure 1(a). As in previous experimental studies, upon $CdCl_2$ treatment, Te atoms at CdTe grain boundaries are substituted by Cl atoms, in Figure 29(a), we substituted Te atoms at the core with Cl, S and P elements, which are designated by 'green' color. To understand the effect of dopant concentration on electronic structure, in Cl substitution case, for the available 6 Te sites at the core we considered 1 Cl, 2 Cl and 6 Cl atoms substituted. The corresponding change in the density of states (DOS) with doping is shown in Figure 29(b). Figure 29(b) clearly shows a large peak at the Fermi level as a result of the dislocation core. When we inserted Cl and increased its concentration, the number of midgap states decreased and if all Te atoms are substituted (6Cl), there we almost no midgap states left and the dislocation core was efficiently passivated. Similarly, passivation effect was also observed if all Te atoms at the core are substituted with S and P atoms. Figure 29(c) shows the radially average electrostatic potential profile around the dislocation core region. For all substituting elements, the electrostatic potential profile did not change drastically compared to the undoped dislocation core. As a result, upon doping, dislocation core still acts as a medium to attract hole carriers,.

In conclusion, we demonstrated that 4.8º (110)||(110) grain boundary can be efficiently passivated by Cl, P and S atoms to reduce the midgap states, and increase the efficiency of CdTe thin film photovoltaics. The effect of Cl has been known, and in this study we propose that P and S incorporation can also be beneficial to improve the CdTe photovoltaic performance.

Deliverables:

Deliverables Task 1 and Task 2: CdTe thin films with doping levels $>10^{15}$ cm^{-3} were demonstrated. A large number of CdTe bi-crystals were fabricated and the effects of interfacial dopants/passivants were demonstrated successfully. The transgranular transport properties and minority carrier lifetimes were successfully measured for passivated and pristine grain boundaries. Deliverables Task 3: Atomic-resolution images, electron energy-loss spectra and X-ray spectra were successfully acquired for high-angle tilt grain boundaries showing the changes in interfacial density of states. The effects of structural units on the density of states was successfully demonstrated. A correlation between the grain boundary structure and position of passivants with recombination losses was developed. Several papers on structural characterization results were published in Scientific Reports, Acta Crystallographica and Applied Physics Letters.[14, 15]

Deliverable for Task 4: First principles DFT modeling was refined for grain boundaries to include high-angle tilt grain boundaries. A list of potential passivants for low and high angle grain boundary structures was successfully determined and the effects were quantified successfully using first-principles DFT models. The stability of individual passivants was determine successfully, as well as the lowest energy position of interfacial passivants in the grain boundary structural units.

Deliverable for Task 5: Bi-crystal grain boundaries were successfully annealed using a variety of approaches. The effects of the different passivation methods was successfully correlated to changes in the minority carrier lifetimes.
Deliverables after 36 months: A low-angle ($\theta = 4°$) and high-angle grain boundary CdTe grain boundary was passivated using $CdCl_2$ and Cd overpressure. However, the minority carrier lifetimes did not improve upon the different annealing and passivation treatments. Several papers were published summarizing the outcomes of this project. New capabilities, experimental as well as theoretical are now available at ANL and UIC. At UIC, the development of atomic-resolution XEDS mapping, which was developed as part of this program on CdTe, now allows the concentration and location of Cl to be determined at the atomic level. These capabilities are available to all users of the UIC Electron Microscopy User Facility. At ANL. The grain boundary software tool, the *Grain Boundary Genie*, is now available for users at the ANL CFN. It was developed as part of this program.

D. OUTLOOK

We have demonstrated the power of combining state-of-the-art synthesis, characterization and first-principles modeling to address fundamental questions in CdTe grain boundaries. We have shown that, for the first time, bi-crystal of CdTe can be fabricated, treated and subsequently characterized. Since grain boundaries have been identified as one of the largest obstacles towards achieving a high energy conversion efficiency in poly-crystalline CdTe devices, bi-crystals, such as the ones fabricated in this project, will be the key to developing a deeper understanding of how grain boundaries limit V_{oc} and the minority carrier lifetimes.

E. PUBLICATIONS RESULTING FROM THIS WORK

"Creating a single twin boundary between two CdTe (111) wafers with controlled rotation angle by wafer bonding," Sun, C., N. Lu, J. Wang, J. Lee, X. Peng, R.F. Klie, and M.J. Kim, *Applied Physics Letters*, **103**, 252104 (2013).

"A New Silicon Drift Detector for High Spatial Resolution STEM-XEDS: Performance and Applications," P.J. Phillips, T. Paulauskas, N. Rowlands, A.W. Nicholls, K.-B. Low, S. Bhadare, R.F. Klie, *Microscopy and Microanalysis*, 2014.

"Creating single boundary between two CdTe (111) wafers with controlled orientation by wafer bonding," C. Sun, N. Lu, G. Lian, J. Wang, X. Peng, R.F. Klie and M.J. Kim, *Microscopy and Microanalysis*, 2014

"Density Functional Theory Modeling of Twin Boundaries in CdTe as Informed by STEM Observations," C. Buurma, T. Paulauskas, Z. Guo, R. Klie, M. K. Y. Chan, *Microscopy and Microanalysis* **20**, 528 (2014).

"Atomic-resolution characterization of the effects of $CdCl_2$ treatment of poly-crystalline CdTe thin films," T. Paulauskas, C. Buurma, E. Colegrove, Z. Guo, S. Sivananthan, M. Chan, R. F. Klie, *Applied Physics Letter* **105**, 071910 (2014).

"Atomic-scale study of polar Lomer-Cottrell and Hirth lock dislocation cores in CdTe," T. Paulauskas, C. Buurma, E. Colegrove, B. Stafford, Z. Guo, M. K. Y. Chan, C. Sun, M. J. Kim, S. Sivananthan, R. F. Klie, *Acta Crystallographica A* **70**, 524 (2014).

"Shockley-Read-Hall lifetimes in CdTe," C. Buurma, S. Krishnamurthy, and S. Sivananthan, *Journal of Applied Physics* **116**, 013102 (2014).

"A Fundamental Study of the Effects of Grain Boundaries on Performance of Poly-Crystalline Thin Film CdTe Solar Cells," T. Paulauskas, C. Buurma, C. Sun, M. K. Y. Chan, M. J. Kim, F. G. Sen, R. F. Klie, *42nd IEEE Photovoltaic Specialists Conference (PVSC)*, (2015). DOI: 10.1109/PVSC.2015.7355937.

"Creation and Analysis of Atomic Structures for CdTe Bi-crystal Interfaces by the Grain Boundary Genie," C. Buurma, F. G. Sen, T. Paulauskas, C. Sun, M. J. Kim, S. Sivananthan, R. F. Klie, M. K. Y. Chan, *42nd IEEE Photovoltaic Specialists Conference (PVSC)*, (2015). DOI: 10.1109/PVSC.2015.7355936.

"Atomistic simulations of grain boundaries in CdTe," F. G. Sen, C. Buurma, T. Paulauskas, C. Sun, M. J. Kim, S. Sivananthan, R. F. Klie, M. K. Y. Chan, *42nd IEEE Photovoltaic Specialists Conference (PVSC)*, (2015). DOI:10.1109/PVSC.2015.7355935.

"Atomic Scale Study of Lomer-Cottrell and Hirth Lock Dislocations in CdTe," T. Paulauskas, C. Buurma, B. Stafford, C. Sun, M. K. Y. Chan, Sivananthan Sivalinghama, M. J. Kim and R. F. Klie, *Microscopy and Microanalysis* **21**, 2087 (2015).

"Atomic and electronic structure of Lomer dislocations at CdTe bicrystal interface," C. Sun, T. Paulauskas, F. G. Sen, G. Lian, J. Wang, C. Buurma, M. K. Y. Chan, R. F. Klie, and M. J. Kim, *Scientific Reports* **6**, 27009 (2016).

"Atomic Scale Study of Model CdTe Grain Boundaries," T. Paulauskas, F. G. Sen, C. Sun, E. Barnard, M. Chan, M. Kim, S. Sivalingham, R. Klie, *43rd IEEE Photovoltaic Specialists Conference (PVSC)* (2016).

"First principles modeling of grain boundaries in CdTe," F. G. Sen, C. Buurma, T. Paulauskas, C. Sun, M. Kim, S. Sivananthan, R. F. Klie, M. K.Y. Chan, *43rd IEEE Photovoltaic Specialists Conference (PVSC)* (2016).

F. BUDGET AND SCHEDULE

The table below shows the project spend plan on a per-quarter basis. The planned and actual spending were very similar.

Calendar Quarter	Year	From	To	A. Federal Share Initial Plan totals $903044	B. Federal Share Updated Actuals & Plan	Cumulative Federal Share	C. Recipient Share Initial Plan totals $xxx	D. Recipient Share Updated Actuals & Plan	Cumulative Recipient Share
Q4	2012	10/1/2012	12/31/2012	$64,457.71	$405.13	$405.13	$0.00	$0.00	$0.00
Q1	2013	1/1/2013	3/31/2013	$64,457.71	$52,813.21	$53,218.34	$0.00	$0.00	$0.00
Q2	2013	4/1/2013	6/30/2013	$64,457.71	$53,166.63	$106,384.97	$0.00	$0.00	$0.00
Q3	2013	7/1/2013	9/30/2013	$64,457.71	$75,704.67	$182,089.64	$0.00	$0.00	$0.00
Q4	2013	10/1/2013	12/31/2013	$64,457.71	$122,469.00	$304,558.64	$0.00	$0.00	$0.00
Q1	2014	1/1/2014	3/31/2014	$64,457.71	$68,138.46	$372,697.10	$0.00	$0.00	$0.00
Q2	2014	4/1/2014	6/30/2014	$64,457.74	$57,964.23	$430,661.33	$0.00	$0.00	$0.00
Q3	2014	7/1/2014	9/30/2014	$0.00	$20,542.67	$451,204.00	$0.00	$0.00	$0.00
Q4	2014	10/1/2014	12/31/2014	$75,306.67	$49,773.00	$500,977.00	$0.00	$0.00	$0.00
Q1	2015	1/1/2015	3/31/2015	$75,306.67	$18,861.14	$519,838.14	$0.00	$0.00	$0.00
Q2	2015	4/1/2015	6/30/2015	$75,306.67	$78,665.65	$598,503.79	$0.00	$0.00	$0.00
Q3	2015	7/1/2015	9/30/2015	$75,306.67	$65,092.00	$663,595.79	$0.00	$0.00	$0.00
Q4	2015	10/1/2015	12/31/2015	$75,306.67	$107,444.00	$771,039.79	$0.00	$0.00	$0.00
Q1	2016	1/1/2016	3/31/2016	$75,306.65	$78,000.68	$849,040.47	$0.00	$0.00	$0.00
Q2	2016	4/1/2016	6/30/2016	$0.00	$27,001.77	$876,042.24	$0.00	$0.00	$0.00
Q3	2016	7/1/2016	9/30/2016	$0.00	$27,001.76	$903,044.00	$0.00	$0.00	$0.00
Q4	2016	10/1/2016	12/31/2016	$0.00	$0.00	$903,044.00	$0.00	$0.00	$0.00
Q1	2017	1/1/2017	3/31/2017	$0.00	$0.00	$903,044.00	$0.00	$0.00	$0.00
Q2	2017	4/1/2017	6/30/2017	$0.00	$0.00	$903,044.00	$0.00	$0.00	$0.00
Q3	2017	7/1/2017	9/30/2017	$0.00	$0.00	$903,044.00	$0.00	$0.00	$0.00
Totals				**$903,044.00**	**$903,044.00**	$903,044.00	**$0.00**	**$0.00**	$0.00

The next table shows the spending category breakdown for expenses budgeted versus actual. Most expenditures are similar to those budgeted, with the exception of supplies and travel.

Object Class Categories Per SF 424a	Approved Budget ($)	Project Expenditures ($) This Reporting Period	Project Expenditures ($) Cumulative
a. Personnel	$239,107	$19,146	$203,624
b. Fringe Benefits	$48,724	$2,157	$26,607
c. Travel	$15,500	$3,490	$42,768
d. Equipment			
e. Supplies	$3,388	-$3,610	$4,063
f. Contractual	$195,000	$12,758	$195,000
g. Construction			
h. Other	$143,617	$4,290	$174,561
i. Total Direct Charges (sum of a to h)	$645,336	$38,230	$646,622
j. Indirect Charges	$257,708	$15,773	$256,423
k. Totals (sum of i and j)	**$903,044**	**$54,002**	**$903,044**
DOE Share			
Cost Share			
Calculated Cost Share Percentage	0.0%	0.0%	0.0%

G. REFERENCES:

[1] NREL. *Best Research-Cell Efficiencies*. 2016; Available from: http://www.nrel.gov/ncpv/images/efficiency_chart.jpg.

[2] Coyle, D.J. *The Effect of Copper on Accelerated Life Test Performance of CdTe Solar Cells*. in *NREL PV Module Reliability Workshop*. 2012. Golden. CO.

[3] Albin, D.S., *Accelerated Stress Testing and Diagnostic Analysis of Degradation in CdTe Solar Cells*, in *2008 SPIE Optics+Photonics Meeting*. 2008: San Diego, CA.

[4] Ferekides, C. and J. Britt, *CdTe Solar Cells with efficiencies above 15%.* Solar Energy Materials and Solar Cells, 1994. **35**: p. 255-262.

[5] Sites, J. and J. Pan, *Strategies to increase CdTe solar-cell voltage.* Thin Solid Films, 2007. **515**(15): p. 6099-6102.

[6] Read, W.T. and W. Shockley, *Dislocation Models of Crystal Grain Boundaries.* Physical Review, 1950. **78**(3): p. 275-289.

[7] Browning, N.D. and S.J. Pennycook, *Direct experimental determination of the atomic structure at internal interfaces.* Journal Of Physics D-Applied Physics, 1996. **29**(7): p. 1779-1798.

[8] Klie, R.F. and N.D. Browning, *Atomic scale characterization of oxygen vacancy segregation at $SrTiO_3$ grain boundaries.* Applied Physics Letters, 2000. **77**(23): p. 3737-3739.

[9] Klie, R.F., J.P. Buban, M. Varela, A. Franceschetti, C. Jooss, Y. Zhu, N.D. Browning, S.T. Pantelides, and S.J. Pennycook, *Enhanced current transport at grain boundaries in high-T_c superconductors.* Nature, 2005. **435**(7041): p. 475-478.

[10] Tochigi, E., Y. Kezuka, N. Shibata, A. Nakamura, and Y. Ikuhara, *Structure of screw dislocations in a (0001)/[0001] low-angle twist grain boundary of alumina (α-Al_2O_3).* Acta Materialia, 2012. **60**(3): p. 1293-1299.

[11] Feng, B., H. Hojo, T. Mizoguchi, H. Ohta, S.D. Findlay, Y. Sato, N. Shibata, T. Yamamoto, and Y. Ikuhara, *Atomic structure of a Sigma 3 [110]/(111) grain boundary in CeO_2.* Applied Physics Letters, 2012. **100**(7).

[12] Mizuno, T., Y. Nagao, A. Yoshikawa, K. Koumoto, T. Kato, Y. Ikuhara, and H. Ohta, *Electric field thermopower modulation analysis of an interfacial conducting layer formed between Y_2O_3 and rutile TiO_2.* Journal of Applied Physics, 2011. **110**(6): p. 06371.

[13] Kim, M., G. Duscher, N.D. Browning, K. Sohlberg, S.T. Pantelides, and S.J. Pennycook, *Nonstoichiometry and the electrical activity of grain boundaries in $SrTiO_3$.* Physical Review Letters, 2001. **86**(18): p. 4056-4059.

[14] Paulauskas, T., C. Buurma, E. Colegrove, B. Stafford, Z. Guo, M.K.Y. Chan, C. Sun, M.J. Kim, S. Sivananthan, and R.F. Klie, *Atomic scale study of polar Lomer-Cottrell and Hirth lock dislocation cores in CdTe.* Acta Crystallographica A - Foundation and Advances, 2014. **70**: p. 524-531.

[15] Sun, C., N. Lu, J. Wang, J. Lee, X. Peng, R.F. Klie, and M.J. Kim, *Creating a single twin boundary between two CdTe (111) wafers with controlled rotation angle by wafer bonding.* Applied Physics Letters, 2013. **103**(25): p. 252104.